South Baltic Wind Atlas

South Baltic Offshore Wind Energy Regions Project

Pena Diaz, Alfredo; Hahmann, Andrea N.; Hasager, Charlotte Bay; Bingöl, Ferhat; Karagali, Ioanna; Badger, Jake; Badger, Merete; Clausen, Niels-Erik

Publication date:
2011

Document Version
Publisher's PDF, also known as Version of record

South Baltic Wind Atlas

South Baltic Offshore Wind Energy Regions Project

Risø-R-Report

Alfredo Peña, Andrea Hahmann, Charlotte B. Hasager, Ferhat Bingöl, Ioanna Karagali, Jake Badger, Merete Badger and Niels-Erik Clausen
Risø-R-1775(EN)
May 2011

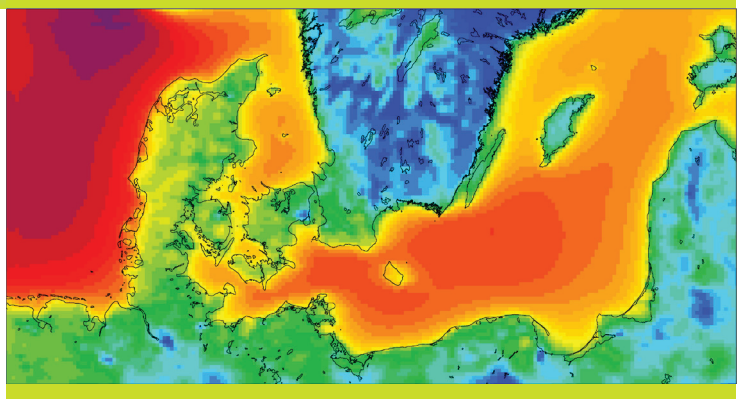

Risø DTU
National Laboratory for Sustainable Energy

Author: Alfredo Peña, Andrea Hahmann, Charlotte B. Hasager, Ferhat Bingöl, Ioanna Karagali, Jake Badger, Merete Badger and Niels-Erik Clausen
Title: South Baltic Wind Atlas
Division: Wind Energy Division

Approved by: Hans E. Jørgensen
Checked by: Hans E. Jørgensen

Risø-R-1775(EN)
May 2011

ISBN 978-87-550-3899-8

Abstract (max. 2000 char.):

A first version of a wind atlas for the South Baltic Sea has been developed using the WRF mesoscale model and verified by data from tall Danish and German masts.
Six different boundary-layer parametrization schemes were evaluated by comparing the WRF results to the observed wind profiles at the masts. The WRF modeling was done in a nested domain of high spatial resolution for 4 years. In addition the long-term wind statistics using the NCAR-NCEP reanalysis data were performed during 30 years to provide basis for a long-term adjustment of the results and the final WRF results include a weighting for the long-term trends variability in the South Baltic Sea.
Observations from Earth observing satellites were used to evaluate the spatial resolution of the WRF model results near the surface. The QuikSCAT and the WRF results compared well whereas the Envisat ASAR mean wind map showed some variation to the others. The long-term analysis revealed that the South Baltic Sea has a spatially highly variable wind climate during the 30-years.

Contract no.:

Group's own reg. no.:
1130610-1-2

Sponsorship:

Cover :

Pages: 66
Tables:
References:

Information Service Department
Risø National Laboratory for Sustainable Energy
Technical University of Denmark
P.O.Box 49
DK-4000 Roskilde
Denmark
Telephone +45 46774005
bibl@risoe.dtu.dk
Fax +45 46774013
www.risoe.dtu.dk

Contents

1 Introduction

The European Commission has identified offshore wind energy as a technology of strategic importance with regards to meet the EU energy and climate targets and a mean for reducing the strong dependency on primary energy imports. The potential for offshore wind energy in Europe is huge and so are the technical challenges related to the implementation; especially wind resource assessment, selection of sites for new projects, wind turbine technology, operation and maintenance, grid integration and investment challenges.

As a mean for promoting and enhancing development of offshore wind energy in the South Baltic Region, the South Baltic Offshore Wind Energy Regions project (South Baltic OFF.E.R) was initiated in March 2010. The project has ten partners from the five countries around the Southern part of the Baltic Sea (for details see http://www.southbaltic-offshore.eu/wind-energy-project-about.html).

The South Baltic OFF.E.R. project addresses the following issues:

- Quicker and more elaborate development of new offshore wind farms
- A cleaner and more secure energy supply for the South Baltic Region
- More and better jobs in the South Baltic Offshore Wind Industry
- Increased competitiveness and strengthened position of the South Baltic Offshore Wind Industry
- Public perception of the South Baltic as one of Europe's premier renewable energy regions
- Lasting cross-border relationships strengthening social cohesion in the region

An important issue when planning offshore wind projects is to know the wind resource. This is one of the five cornerstones of Wind Farm Planning: wind resource, environment and social acceptance, grid connection, project economy and political support.

The present report describes the offshore wind resources in the South Baltic area and is a deliverable of the South Baltic Offshore Wind Energy Regions project.

The European Wind Atlas (Troen and Petersen, 1989) include a map for offshore, see http://www.windatlas.dk/Europe/oceanmap.html partly covering the South Baltic Sea based on information prior to 1989. In the Northern Baltic Sea winds have been studied in the 1990s (Niros et al., 2002) and winds in the entire Baltic Sea have been studied in the period 1960 to 1990 (Mietus, 1998) The information for the 1960 to 1990 period is based on mainly ship and lighthouse data. The resulting map on mean wind speed for this period is shown in Figure 55 (for comparison with Synthetic Aperture Radar results).

The report consists of nine main sections:

Section 2 Methodology This section outlines the methodology applied in the present report including the model set-up, the domain and the parameterizations used for the WRF (Weather Research and Forecasting model) simulations and the use of satellite observations and meteorological data.

Section 3 WRF Oct 2009 A preliminary evaluation of several planetary boundary layer parameterizations in the WRF model is performed with data from meteorological masts in the North and Baltic Seas.

Section 4 Wind classes The set of wind classes represent the different wind conditions (sets of wind speed, direction and atmospheric stability) for a long-term period. The wind classes are defined from long term, large scale atmospheric reanalysis datasets. In this study 30 years of the NCEP-DOE Reanalysis 2 are used covering the period 1980–2009. The wind classes are used to apply long-term weights to the four years of meso-scale simulations using WRF and thereby extending the validity to the long-term period applied.

Section 5 Validation The four years of meso-scale simulations by WRF are validated against observations from offshore and onshore meteorological data at different levels.

Section 6 QuickSCAT The section outlines the wind resource based on satellite images obtained from NASA's QuikSCAT mission, which was operational from July 1999 until November 2009.

Section 7 SAR The section outlines the wind resource assessment based on satellite images obtained from ESA's Envisat satellite using advanced synthetic aperture radar. The wind maps obtained by ASAR can be obtained at around 1 km by 1 km resolution and near the coast (2–3 km).

Section 8 Wind atlas The wind atlas of the South Baltic region is generated based on the 4 year WRF simulations and the long-term correction based on the wind classes approach.

Section 9 Observed wind climate at Fino2 The results of the observed wind climate at Fino2 are shown as an example of the type of results that the WRF run can provide for the whole South Baltic region.

2 Methodology

2.1 WRF simulations

Because the region of interest is deficient of a good observational network focused on wind measurements, we rely on the use of a numerical weather prediction model to generate a high-resolution long-term wind climatology of the South Baltic area. The dynamical downscaling used in this study uses the technique developed by Hahmann et al. (2010), but using Newtonian relaxation towards the large scale analysis (also known as grid nudging or analysis nudging).

The model used is version 3.2.1 of the Advanced Research WRF (Weather Research and Forecasting) model. Details of the model can be found in Skamarock et al. (2008). The model setup is described in Table 1, except for the various surface, boundary layer, and land surface parameterizations used in the sensitivity experiments. It is worth noting that the grid used has been rotated to better cover the region of interest as shown in Figure 1. Figures 2 and 3 show the terrain elevation and landuse used in the simulations. The terrain is derived from USGS (United States Geological Service) 30" spatial resolution data. The landuse is derived from Moderate Resolution Imaging Spectroradiometer (MODIS) at 30" with 20 categories.

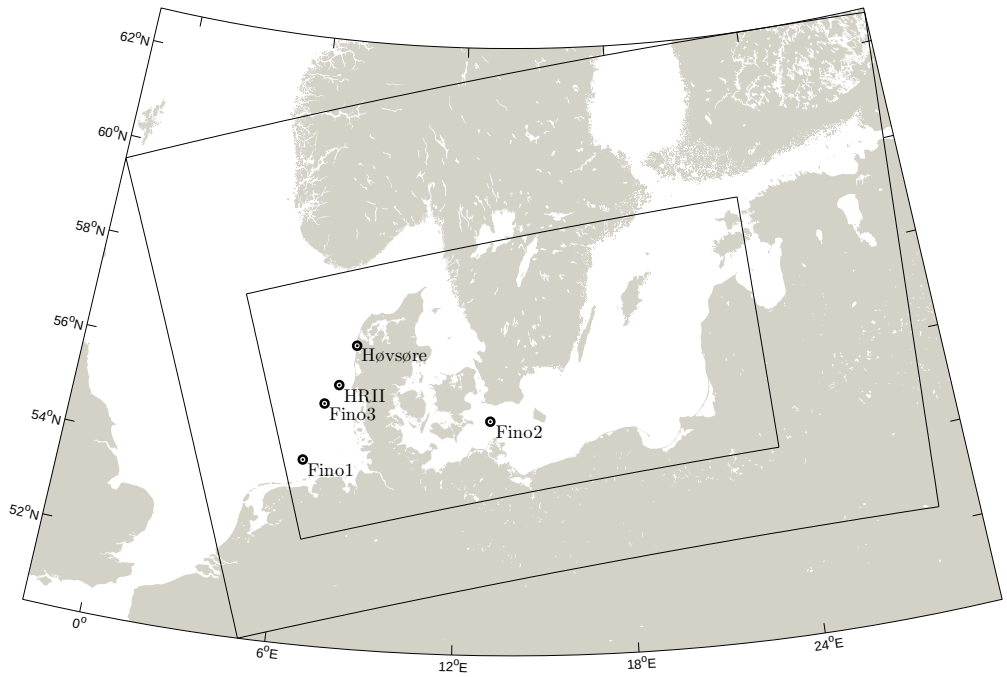

Figure 1: Location of the WRF model domains and meteorological masts used in the verification of the results.

Time series of wind speed and direction extracted from the model output are later verified against observations (see Section 5). Since most verifying sites are located offshore, the grid point chosen for the extracted time series is simply the one closest to the observation coordinates.

2.2 Observations

Observations from tall meteorological masts and from Earth observation satellite data are used for comparison to the WRF model results. The meteorological masts include Fino1,

Table 1: Summary of model and system setup, and physical parameterizations used in the WRF simulations.

Model setup:
WRF (ARW) Version 3.2.1.
Mother domain (D1; 102×70 grid points) with 15 km resolution; 1 nested domain (D2; 205×106) using 5 km horizontal resolution on a polar stereographic projection (see Figure 1).
41 vertical levels with model top at 50 hPa; 12 of these levels are placed within 1000 m of the surface; the first level is at approximately 14 meters AGL.
MODIS land-cover classification of the International Geosphere-Biosphere Programme.
Simulation setup:
Initial, boundary conditions, and fields for grid nudging come from the NOAA Climate Forecast System Reanalysis (CFSR; (Saha et al., 2010)) at $0.5^\circ \times 0.5^\circ$ resolution.
Runs are started (cold start) at 00:00 UTC every 10 days and are integrated for 11 days, the first 24 hours of each simulation are disregarded.
Sea surface temperature (SST) and sea-ice fractions come from the dataset of Reynolds et al. (2002) with $0.25^\circ \times 0.25^\circ$ resolution, updated daily.
Model output: hourly, wind speeds every 10 minutes.
One-way nested domains.
Grid nudging on D1 only and above level 10; nudging coefficient 0.0003 s^{-1} for wind, temperature and specific humidity.
Physical parameterizations:
Precipitation: Thompson graupel scheme (option 8), Kain-Fritsch cumulus parametrization (option 1)
Radiation: RRTM scheme for longwave (option 1); Dudhia scheme for shortwave (option 1)
PBL and land surface: Mellor-Yamada-Janjic scheme (Mellor and Yamada (1982), option 2), Eta similarity (option 2) surface layer scheme, and Noah Land Surface Model (option 2). Sensitivity experiments were conducted in Section 3.
Diffusion: Simple diffusion (option 1); 2D deformation (option 4); 6th order positive definite numerical diffusion (option 2); rates of 0.06, 0.08, for D1 and D2, respectively; no vertical damping.
Positive definite advection of moisture and scalars.

Fino2 and Fino3 in Germany. These three masts are located offshore. The meteorological mast Høvsøre in Denmark is located 1.7 km from the coast of the North Sea in Denmark. Lidar observations at Horns Rev (HRII) has also been used. This is from an offshore wind farm. Figure 1 shows the location of the meteorological observations. Section 5 describes the comparisons of the WRF model and the meteorological data.

The satellite observations include 10-yr of twice daily QuikSCAT ocean wind vector observations from Remote Sensing Systems. The data are from the SeaWinds scatterometer on-board the QuikSCAT satellite belonging to NASA. Section 6 describes the details.

Envisat ASAR (Advanced Synthetic Aperture Radar) scenes from the European Space Agency (ESA) has been retrieved and processed at Risø DTU. Section 7 describes the details.

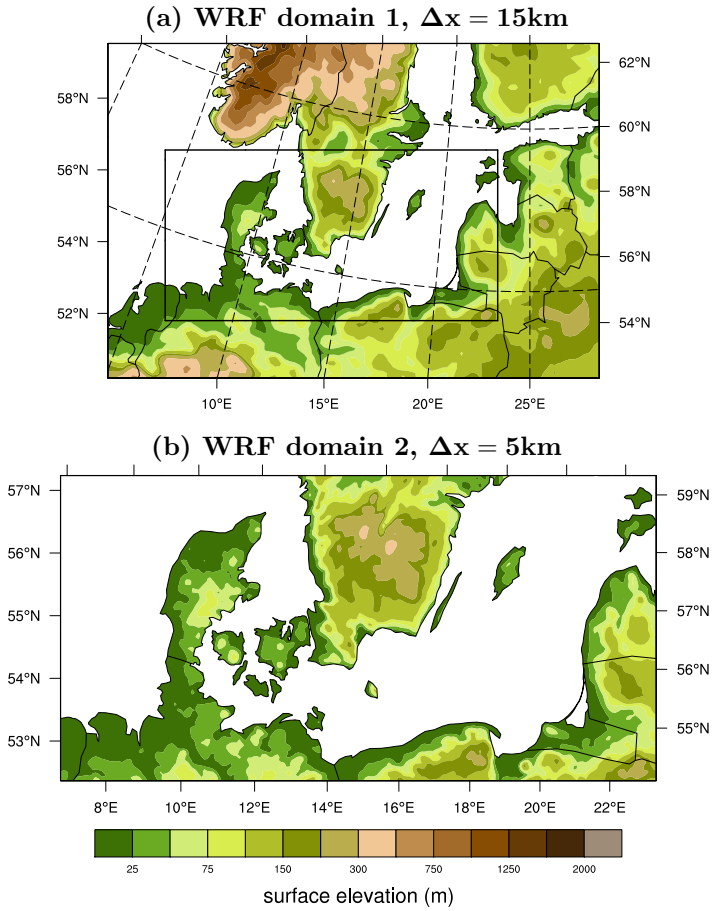

Figure 2: Terrain elevation (m) used in the WRF simulations for: (a) Domain 1, $\Delta x = 15$ km; and (b) Domain 2, $\Delta x = 5$ km.

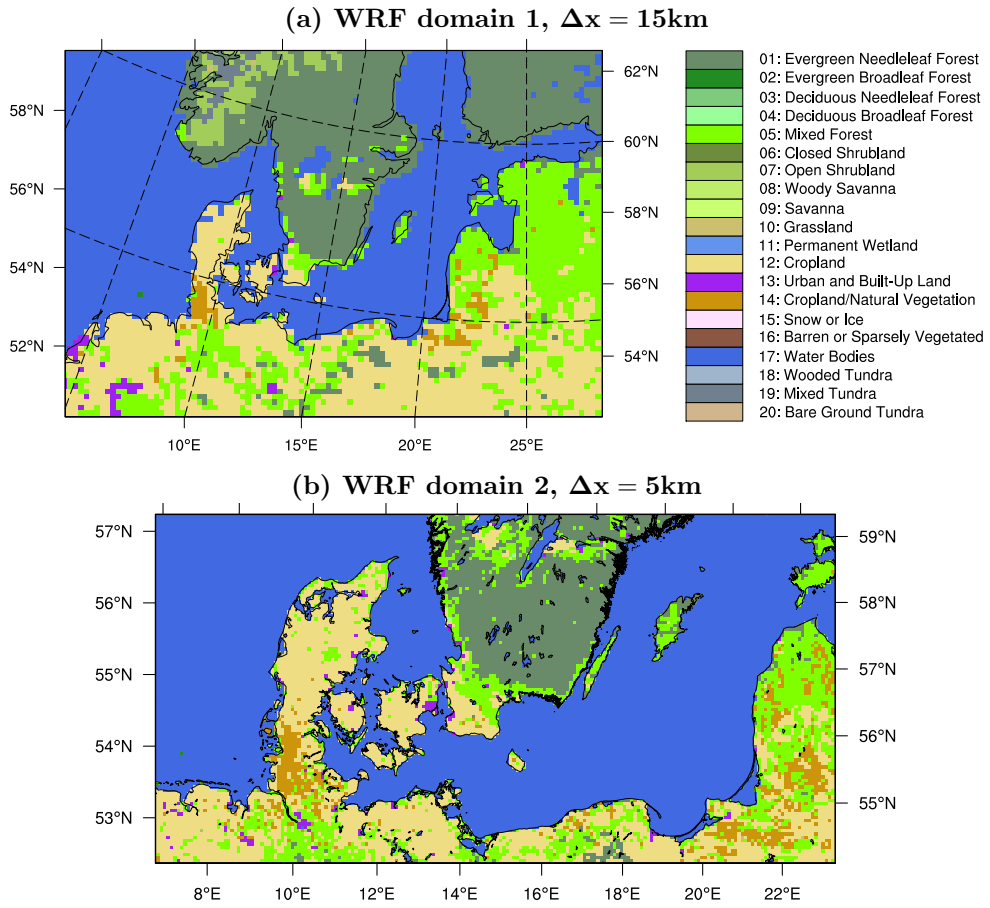

Figure 3: Landuse classes used in the WRF simulations for: (a) Domain 1, $\Delta x = 15$ km; and (b) Domain 2, $\Delta x = 5$ km.

3 WRF Oct 2009

A series of sensitivity experiments were conducted to find the optimal model setup for the model simulations. The experiments concentrated on the choice of planetary boundary layer parametrization. The model configuration is as presented in Section 2.1 and in Table 1.

3.1 Experiments

Eight PBL parameterizations are available for use within WRF. Six of these can be used with the Noah LSM land surface scheme ad the MODIS land-cover types.

Table 2: Summary of PBL schemes used the model sensitivity study.

Scheme	*Reference*	*Closure type*	*Surface scheme*
YSU	Hong et al. (2006)	1st order	M-O scheme
MYJ	Janjic (2001)	TKE 1.5 order	M-O scheme
QNSE	Sukoriansky et al. (2006)	TKE 1.5 order	QNSE
MYNN2	Nakanishi and Niino (2006)	TKE 1.5 order	MYNN
MYNN3	Nakanishi and Niino (2006)	TKE 2.5 order	MYNN
BouLac	Bougeault and Lacarrère (1989)	TKE 1.5 order	M-O scheme

The experiments consisted of month-long simulations for the period 1–30 October 2009, using the model configuration described in section 2, except for the 6 different PBL and their respective surface layer schemes listed in Table 2.

3.2 Comparison and validation of sensitivity experiments

We verify the vertical profiles of wind speed simulated by WRF using the seven simulations against data from meteorological masts and lidar. To examine the spatial distribution of model-simulated winds, we also verify against data from QuikSCAT.

To compare the time series of wind speed derived from the WRF model and those from the observations, we use pairs of WRF and measurements only when both are available. Also, we only use observations that are not influenced by the wake of the wind turbines at Høvsøre (i.e. wind speeds whose directions are between 345°–15° are not used) and not influenced by the mast boom: 295°–340° at Fino1 and 350°–20° at Fino2.

The results in Table 3 and Figure 4 show that in general it is not possible to find one single scheme that performs better than the others under all conditions, sites, and metrics. For example, if we consider the mean column wind speed, the MYNN3 scheme performs better (i.e. has the lowest BIAS and RSME) at Høvsøre but the BouLac scheme performs best at Fino1 and Fino2. Similar results are found for the tall wind speed at (100 m at Høvsøre; 90 m at Fino1 and Fino2). Therefore, other metrics such as wind shear and wind speed variability should be used in conjunction with the statistics used here. In addition, Draxl et al. (2011) showed that the performance of each PBL scheme is highly dependent on the boundary layer stability conditions.

Figure 4 shows the mean wind speed (1–30 June 2009) as a function of height for all six PBL schemes and the observations at Fino1, Fino2, and Høvsøre. The spread among PBL schemes is, as expected, lower for the two ocean sites than for Høvsøre, which is located over land. Differences between the model-derived wind speeds and the observations are of the order of 0.5 m s^{-1} at Fino1 and Fino2, but much larger ($\sim$1.5 m s^{-1}) at Høvsøre. When considering the "slope" and "shape" of the wind profile simulated by the models and compared to the observations, at Fino1 YSU performs best, at Fino2 MYJ is perhaps

Table 3: Bias and RMSE (m s^{-1}) between observed and model simulated wind speeds at three masts presented in Figure 1. The "mean column" represents the mean of the statistic (i.e. BIAS or RMSE) over all levels (30–100 m). The second set of statistics is for a single level at 90 m at Fino1 and Fino2 and 100 m at Høvsøre. The lowest value among the different PBL schemes is in blue; the highest in red.

Mean column wind speed

Scheme	*Høvsøre BIAS*	*Fino1 BIAS*	*Fino2 BIAS*	*Høvsøre RMSE*	*Fino1 RMSE*	*Fino2 RMSE*
YSU	0.11	0.38	0.47	3.32	3.01	3.48
MYJ	-0.28	0.01	0.32	3.01	3.15	3.13
QNSE	-0.39	-0.03	0.47	3.40	3.37	3.95
MYNN2	-0.15	0.13	0.42	3.23	3.18	3.51
MYNN3	-0.10	0.30	0.43	2.89	3.19	3.71
BouLac	0.17	0.02	0.11	3.84	2.96	2.87

90 or 100-meter wind speed

Scheme	*Høvsøre BIAS*	*Fino1 BIAS*	*Fino2 BIAS*	*Høvsøre RMSE*	*Fino1 RMSE*	*Fino2 RMSE*
YSU	-0.22	0.38	0.59	0.67	0.46	0.60
MYJ	-0.24	0.05	0.45	0.65	0.49	0.55
QNSE	-0.17	0.01	0.62	0.72	0.51	0.68
MYNN2	-0.12	0.08	0.50	0.70	0.48	0.59
MYNN3	-0.10	0.24	0.50	0.63	0.48	0.62
BouLac	-0.35	0.01	0.22	0.76	0.44	0.49

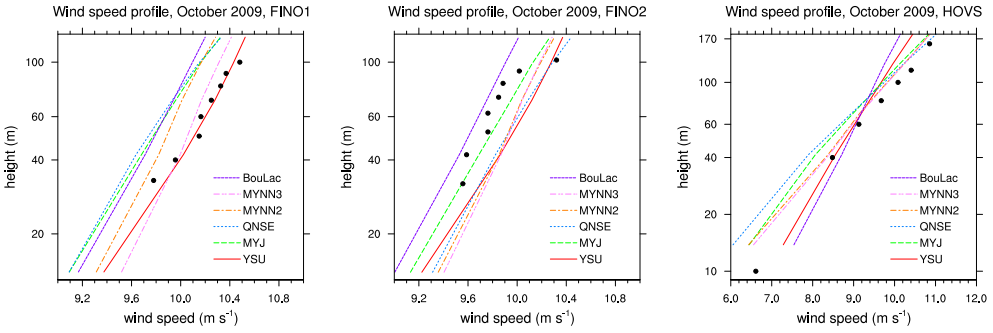

Figure 4: Vertical profiles of wind speed (m s^{-1}) simulated by WRF using the six PBL parameterizations in Table 2 compared to measurements at Fino1, Fino2, and Høvsøre. Profiles represent the average for the period 1–30 October 2009. Wind speeds whose directions are affected by wind farm wake (Høvsøre) or mast booms (Fino1 and Fino2) have been removed from both observations and models.

the best, and at Høvsøre the MYNN3 seems to outperform the others, in agreement with the results in Table 3.

The difference in behavior among the different PBL schemes between land and ocean is emphasized by the results in Figure 5. The figure shows the differences in wind speed at three model levels (approximately located at 42, 99, and 127 m above ground) between simulations using the YSU and MYJ PBL schemes. While at 42 m the simulation using YSU always has stronger winds than that using MYJ, especially over land, winds are stronger in the simulation using MYJ than that using YSU at 127 m over land. This general trend is partly visible in the vertical wind speed profiles shown in Figure 4.

A comparison of the mean biases and RMSE of the 10-m wind speeds in the various WRF simulations as compared to the QuikSCAT data is shown in Figures 6 and 7. In

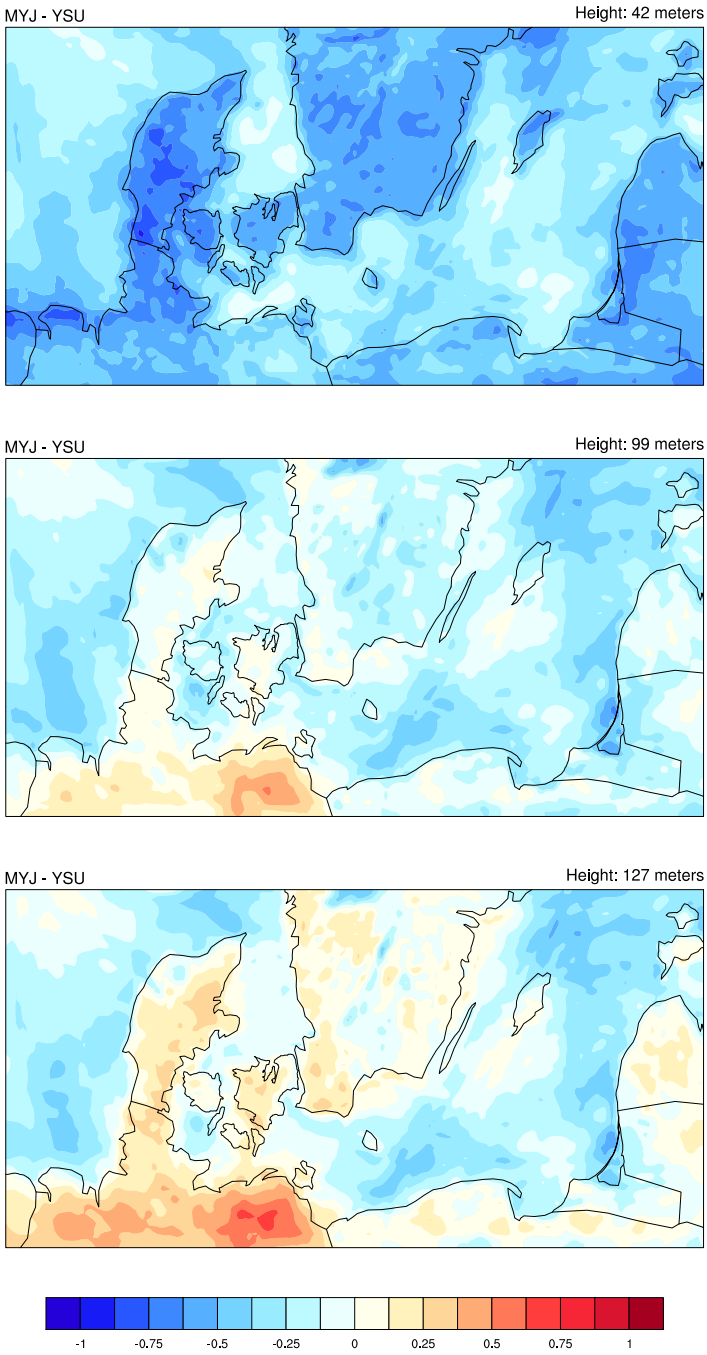

Figure 5: Differences in mean wind speed ($\mathrm{m\,s^{-1}}$) between two month-long simulations using WRF with different PBL schemes (MYJ minus YSU) at: 42 m (top), 99 m (middle), and 127 m (bottom).

general, the mean biases are very similar among the simulations. Over the North Sea and most of the Baltic Sea 10-m wind speeds simulated by WRF are within $\pm$ 1 m $\mathrm{s^{-1}}$ of those observed. Over the eastern coast of Poland, Russia and Lithuania biases are slightly larger (1–2 m $\mathrm{s^{-1}}$) in all simulations. Small areas with negative biases (i.e. WRF wind speeds larger than observed) occur in the MYNN2 and MYNN3 simulations over the western Baltic Sea.

The RMSE errors between WRF simulations and QuikSCAT observations are also quite similar among the various schemes. Most areas show RMSE $<$ 2.5 m $\mathrm{s^{-1}}$. As seen

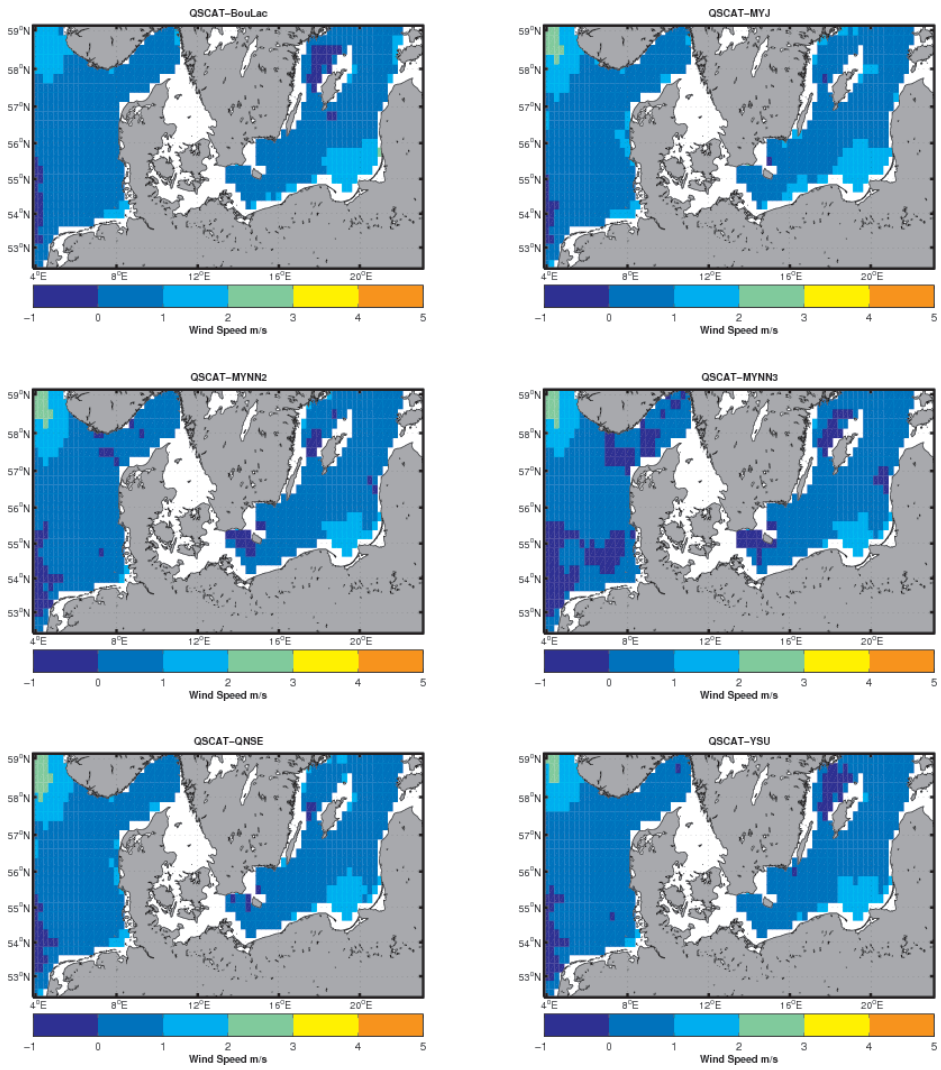

Figure 6: Bias (m s^{-1}; QuikSCAT minus WRF) in 10-m wind speed between the monthly-averaged (1–30 October 2009) WRF results and those derived from QuikSCAT. The WRF 10-m wind speeds were derived from extrapolating the wind speed values from the first 3 WRF levels. WRF values were interpolated to the QuikSCAT grid and only times available in both datasets are used.

in the biases, the RMSE are slightly larger along the southeastern Baltic coast (2.5–3.5 m s^{-1}) and the western Danish coast. Since the QuikSCAT represents "neutral" winds (i.e. winds that are extrapolated from the sea surface to 10 m using a neutral logarithmic profile) some of these errors are a consequence of differences in stability between the model simulations and the observations. Much larger errors are seen in the northwest corner of the domain. The reason for these is unknown.

Based on these maps it is not at all clear which PBL outperforms the others. Indeed, a choice made only on these results could have been misleading. Clearly, good performance at 10 m, does not guarantee good agreement further up in the boundary layer (see Figure 4 and 5).

Based on the performance at all three sites and for the four statistics, we chose to perform the long term simulations for the wind atlas of the South Baltic using the MYJ PBL scheme. The results of a parallel study by Draxl et al. (2011) indicate that this is a good choice also in terms of the mean wind shear, represented by the shear-exponent,

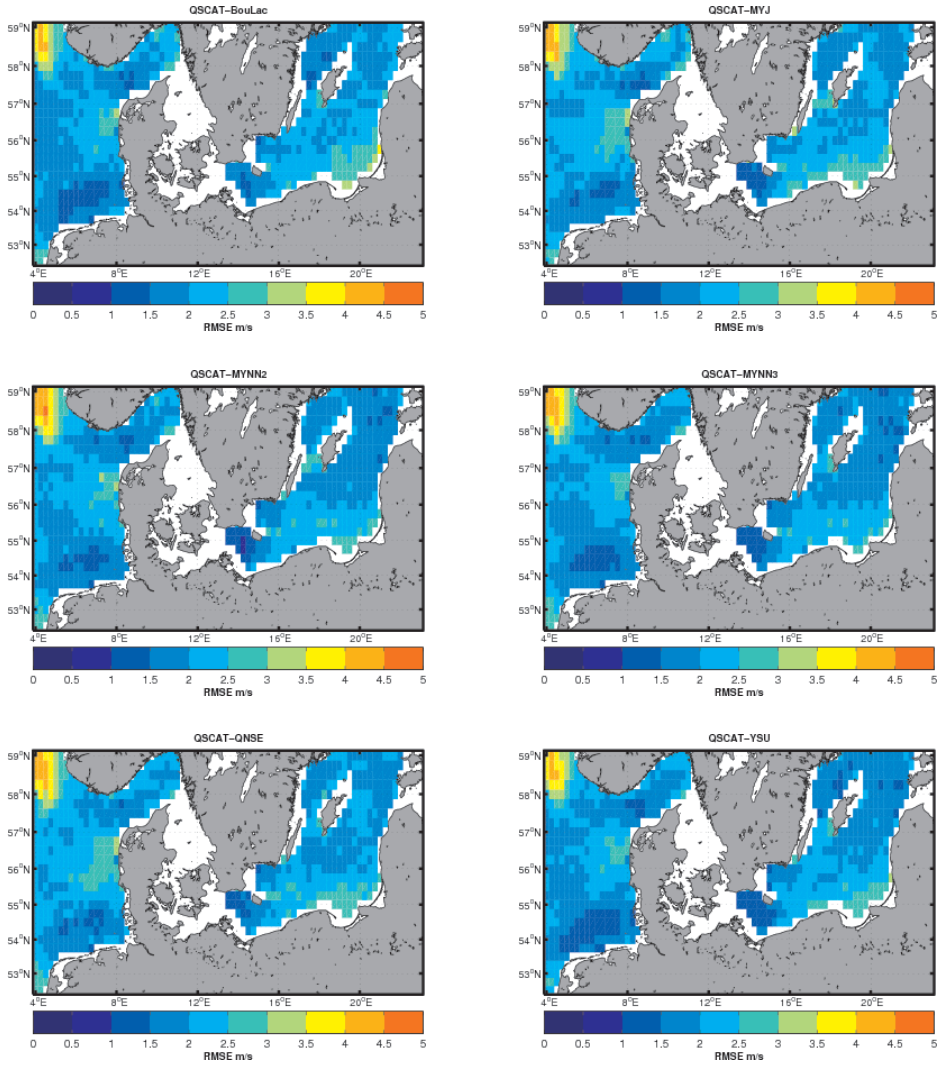

Figure 7: RMSE (m s^{-1}) in 10-m wind speed between WRF-derived winds and those derived from QuikSCAT. The WRF 10-m wind speeds were derived from extrapolating the wind speed values from the first 3 WRF levels. WRF values were interpolated to the QuikSCAT grid and only times available in both datasets are used.

and its temporal variability.

4 Wind classes

The usual procedure for calculating wind resource with the numerical wind atlas method involves, as a first step, the definition of a set of wind classes. The set of wind classes represent the different wind conditions (wind speed, direction and atmospheric stability) for a climatological period. The wind classes are defined from long term, large scale atmospheric reanalysis datasets. In this study 30 years of the NCEP-DOE AMIP-II (often referred to as NCEP-DOE Reanalysis 2) are used covering the period 1980–2009 (Kanamitsu et al., 2002).

The original purpose of the wind class approach was to create a set of representative atmospheric conditions and run a mesoscale model with these conditions. This, so-called, statistical-dynamical approach, allows wind climate statistic to be estimated efficiently in terms of computer resource, see Frank et al. (2001) and Nygaard et al. (2010) for numerical wind atlas study examples.

The wind classes are based on geostrophic wind and potential temperature at 0, 1500, 3000, 5500 m above sea level. The NCEP-DOE Reanalysis 2 geopotential height, temperature, and specific humidity data are used on for the data covering the geographical area 7.5–25 E 52.5–60 N at 2.5 degree grid spacing. The geostophic wind is based on centred differencing of geopotential height calculated at reanalysis grid 'mid-points', giving a 2.5 degree spaced grid from 8.75–23.75 E 53.75–58.75 N.

The wind classes are usually defined by the distribution of wind speed, direction and stability at one point. For the South Baltic wind atlas the area of interest is 10.5–21.5 E 54.0–58.0 N. This is a large area of interest and it is therefore of interest to see how well wind classes defined at one 'mid-point' manage to represent the large scale climate over this large area. There are two main issues, i. do wind classes represent the large scale wind climate well over the entire region of interest and ii. to what extent can a single wind class describe the wind in the region at any given time.

Initially four sets of wind classes were defined, all based on the large scale conditions at 'mid-point' 16.25E 56.25N. Figure 8 shows the four sets of wind classes. The sets, named SB1, SB2, SB3, SB4 contain 134, 84, 84, 36 wind classes respectively. Sets SB1, SB2, SB4 differ in that a different number of wind classes is allowed for each of the 12 direction sectors (14, 7, 3 respectively) but in each sector the wind speed range of each wind class varies so as to obtain wind classes with approximately equal frequency of occurrence. The advantage of this is that each wind class is equally important, and that within the numerical wind atlas mmethodology, the computer resource employed for mesoscale simulations is distributed evenly. In contrast, wind class set SB3 uses 7 wind classes per sector, but the wind speed range is fixed and this means that the frequency of each wind class varies within each sector.

The graphs in Figure 8 illustrate the how the same large scale wind climate can be expressed in terms of different wind classes sets. In each case the description is the same, that is the most frequent sectors are the westerly sectors, and it is these sectors that exhibit the strongest geostrophic winds. Also the stability tends to be slightly higher for the easterly wind sectors compared to the westerly sectors.

The first question to address is, how well do the wind classes represent the large scale wind climate over the South Baltic. The answer is given in Figures 9, 10, 11 and 12. The maps show the geostrophic wind speed at 0 (sea level), 1500, 3000, 5500 m over the region of interest and the ratio of the mean of the geostrophic wind speed cubed derived from wind classes for sets SB1, SB2, SB3 and SB4, over that calculated directly from the time series. The mean of the wind speed cubed is of interest, because the wind power density is proportional to this.

Over the South Baltic at sea level the geostrophic wind drops from 9.8 m s^{-1} in the west to 9.2 m s^{-1} in the east. The 134 wind classes of set SB1 capture the wind power in the large scale climate quite accurately with only a small error of less than 3% in the

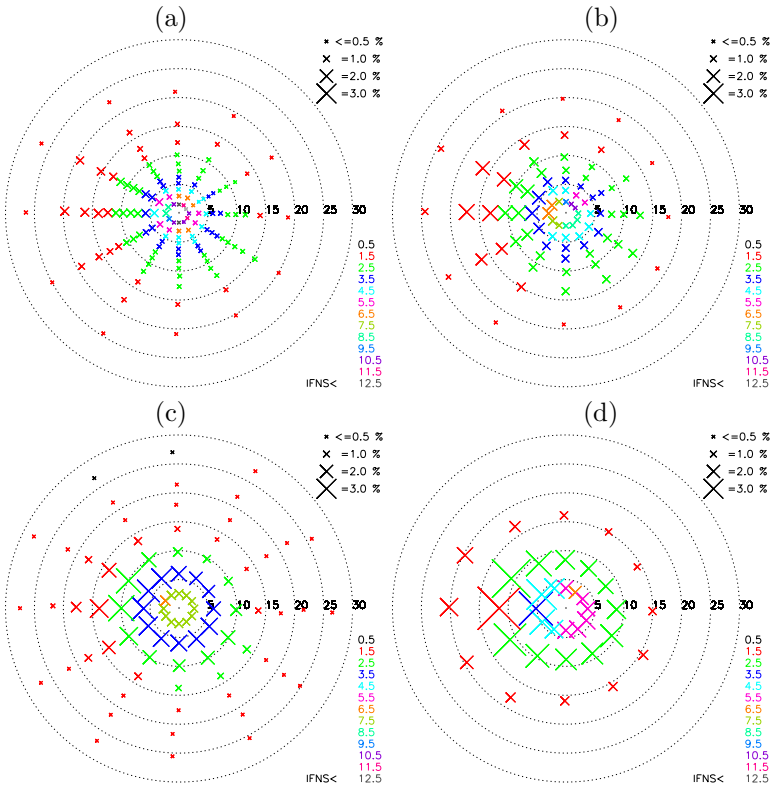

Figure 8: Four sets of wind classes (a) SB1, (b) SB2, (c) SB3 and (d) SB4. Each cross represents a forcing wind speed (distance from the centre of the diagram) and direction. The speed scale is in m s^{-1}. The colours indicate the inverse Froude number squared (IFNS).

mean of the wind cubed. Wind classes sets SB2 and SB3 give an error in the region of 5% on the mean of the wind cubed. Whereas the 36 wind classes of set SB4 do more poorly, with an error in the region of 14% in the mean of the wind speed cubed.

A characteristic of the wind class method is that the 0 m large scale winds are most accurately represented, but moving up from 0 m the large scale winds become more poorly represented. This is evident in Figures 9, 10, 11 and 12b, c and d.

At 1500 m, the geostrophic wind drops from 10.0 to 9.4 m s^{-1}, moving eastwards over the area of interest. At 3000 m, the geostrophic wind drops from 11.7 to 11.1 and at 5500 m, the drop is from 16.7 to 15.9 m s^{-1}. Wind class set SB1 obtains an accuracy of around 9, 20, 35% on the mean of the wind speed cubed for 1500, 3000 and 5500 m respectively. For SB2 the accuracy for the same heights is 10, 21, 35%. For SB3 the figures are 9, 21, 35% and for SB4 the figures are 17, 25, 37%. This shows that use of fewer wind classes makes little impact on the accuracy at 3000 and 5500 m. However, at 1500 m the accuracy is better for the SB1 (134 wind classes), poorer for SB2 and SB3 (84 wind classes) and poorer still for SB4 (36 wind classes).

The next issue to address concerns to what extent it can be expected that a single wind class, at any given time is influencing the whole area of interest. Figure 13 shows the correlation of geostrophic wind speed at sea level at 16.25E 56.25N (Figure 13a), 11.25E 56.25N (Figure 13b) and 21.25E 56.25N (Figure 13c) with neighbouring reanalysis grid mid-points. It shows there is strong correlation over some of the South Baltic. This is associated with the weather systems that pass over the area of interest. The pattern of the correlation reflects the characteristic scale of the mid-latitude low pressure systems that predominately influence the region.

But consideration of wind speed alone, gives no consideration to wind direction. On the otherhand, wind classes allow a kind of 'correlation' of wind speed and direction

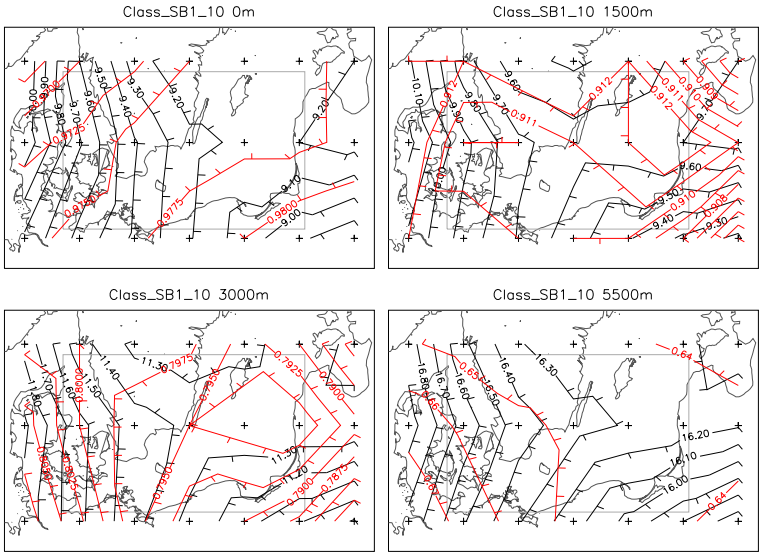

Figure 9: Evaluation of SB1: geostrophic wind speed at sea level as given by NCEP/NCAR reanalysis data 1980–2009 (black contours) and the ratio of the mean of geostrophic wind speed cubed derived from wind classes over that calculated directly for wind class sets (red contours)

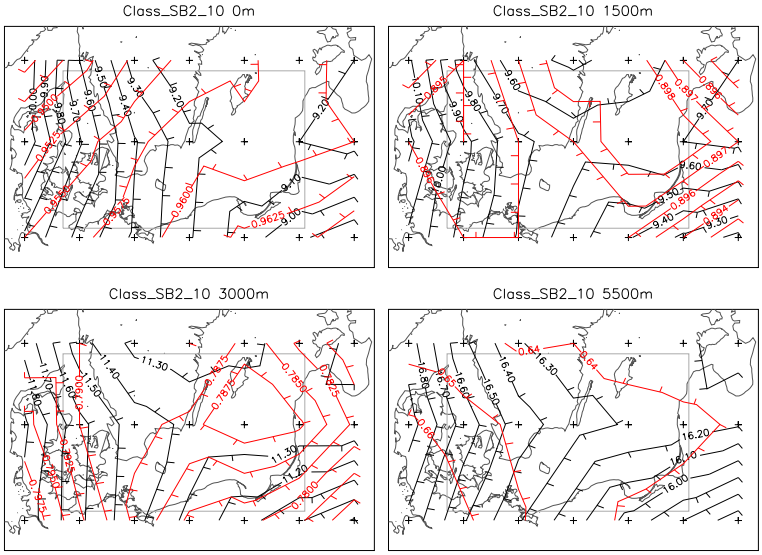

Figure 10: Evaluation of SB2: geostrophic wind speed at sea level as given by NCEP/NCAR reanalysis data 1980–2009 (black contours) and the ratio of the mean of geostrophic wind speed cubed derived from wind classes over that calculated directly for wind class sets (red contours)

to be considered too. Figure 14a, b, c show the probability of locations in the South Baltic experiencing the same wind class as 16.25E 56.25N, 11.25E 56.25N and 21.25E 56.25N respectively, at any time for any wind class, based on wind class set SB1. It can be seen that the probability rapidly drops off when moving away from the reference point. Neighbouring mid-points west and east have a probability of 20-30% of having the same wind class. Neighbouring mid-points north and south have a probability of 10-20% of having the same wind class.This difference in the rate of drop off of probability when moving longitudinally compared to latitudinally is also seen in the wind speed correlation maps in Figure 13.

It is interesting to see the effect of filtering cases when a wind class persists over a

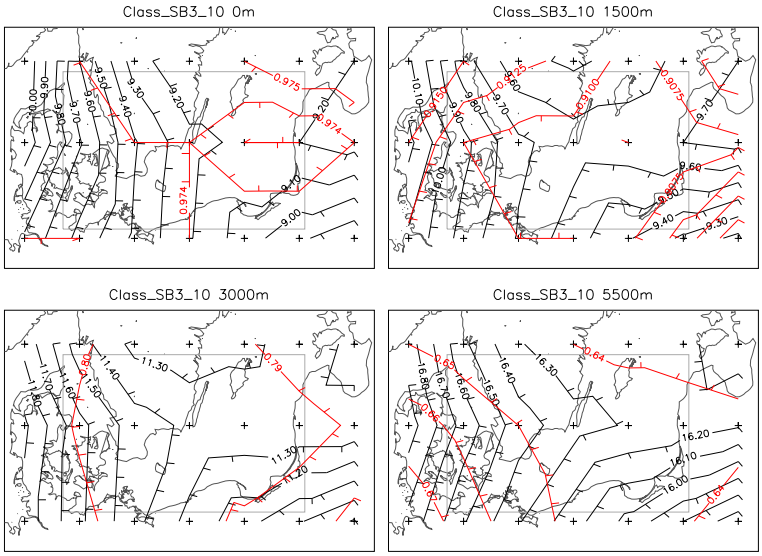

Figure 11: Evaluation of SB3: geostrophic wind speed at sea level as given by NCEP/NCAR reanalysis data 1980–2009 (black contours) and the ratio of the mean of geostrophic wind speed cubed derived from wind classes over that calculated directly for wind class sets (red contours)

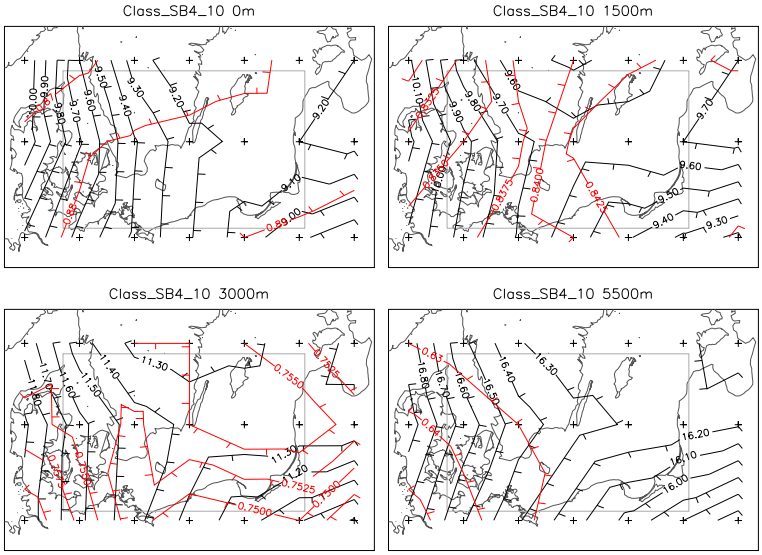

Figure 12: Evaluation of SB4: geostrophic wind speed at sea level as given by NCEP/NCAR reanalysis data 1980–2009 (black contours) and the ratio of the mean of geostrophic wind speed cubed derived from wind classes over that calculated directly for wind class sets (red contours)

period of 6 or 24 hours. Figure 15 shows the probability of the same wind class for persistence of 6 or 24 hours. A longer persistance is associated with a reduction in the drop off of probability. For the 6 hour persistence moving to mid-points west or east gives 30-40% probabilities. Moving north or south still gives 10-20% probabilities. For 24 hour persistencewhen moving west or east the probability is 60-70%, moving north or south the probability is 20-50%. Thus a temporally persistent wind class is associated with a larger spatial extent of a wind class. However, the whole region of interest cannot be described as having a single wind class acting over it.

The same conclusion is true for the wind classes sets SB2, SB3 and SB4 see Figures, 16, 17 and 18. However, it can be noted that the drop off of probability of locations having

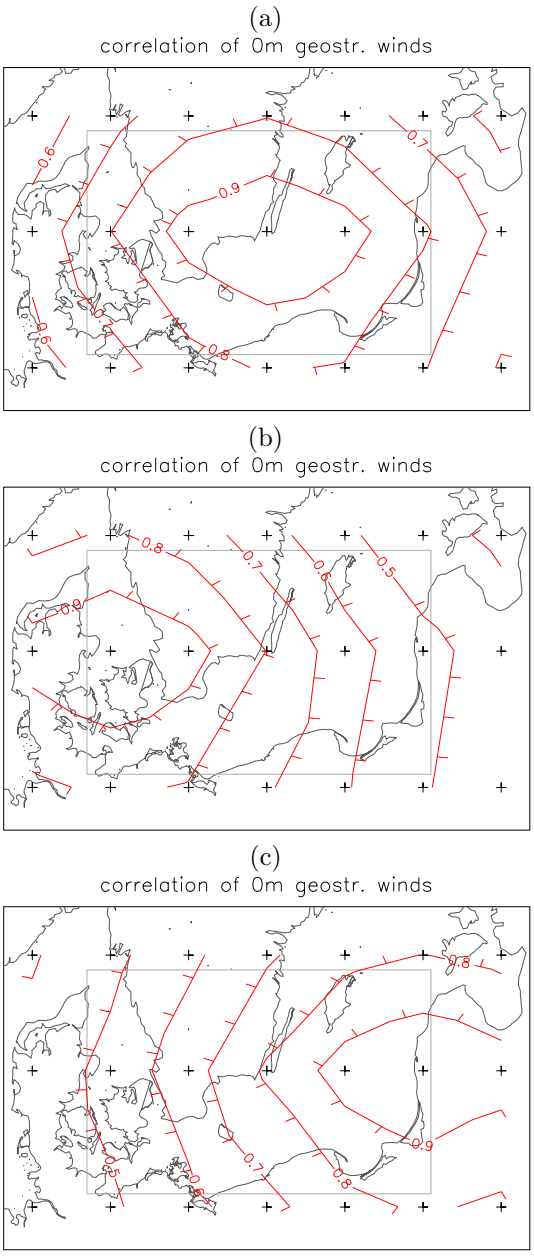

Figure 13: Correlation of geostrophic wind speed at sea level at (a) 16.25E 56.25N, (b) 11.25E 56.25N, (c) 21.25E 56.25N,, with neighbouring reanalysis grid points (marked by + symbols) .

the same wind class is more rapid when there are more wind classes, i.e. SB1 compared to SB4, and slightly more rapid when varying wind speed ranges for wind classes are used, i.e. SB2 compared to SB3.

With such a large region of interest, it is important to define a wind class set that is relevant for the whole region. It has been shown that defining wind classes according to the large scale winds at one location (as has been done here for SB1, SB2, SB3 and SB4, using the mid-point 16.25E 56.25N), does not introduce a large error in the represention of the large scale wind power climate (less than 3% for SB1). However, it cannot be ensured that the wind classes have equal relevance around the domain. For example, some large scale wind situations may be poorly represented by a wind class set determined at another location. To combat this, a final wind class set, SB5, was determined with the same configuration as SB1 (i.e. giving 134 wind classes), but using the large scale data

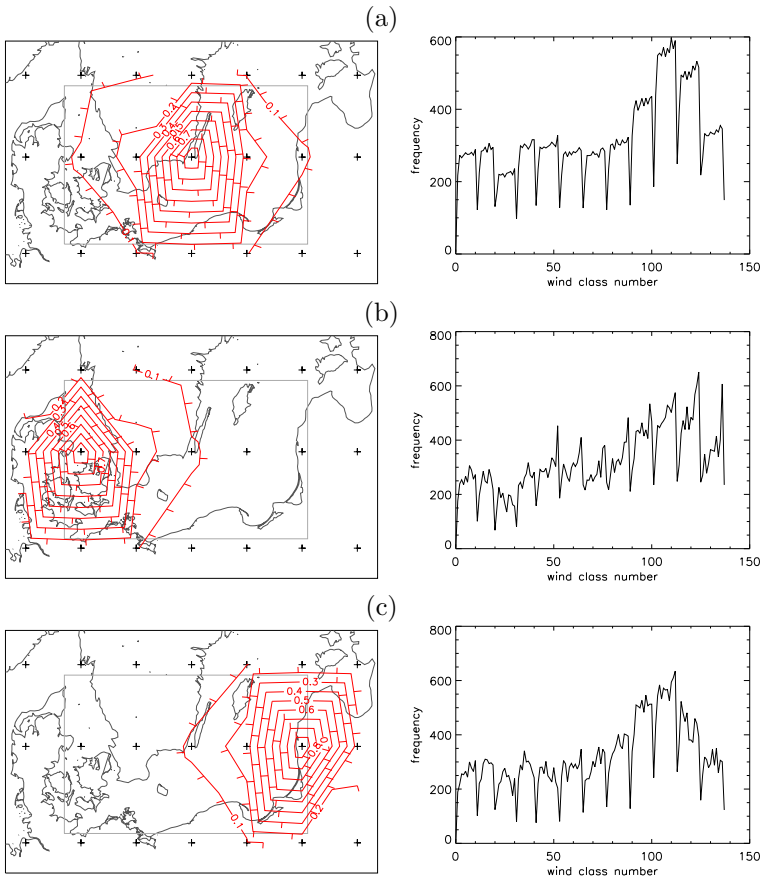

Figure 14: Maps showing the probability of the wind class at (a) 16.25E 56.25N (b) 16.25E 56.25N (c) 16.25E 56.25N being the same as the wind class at neighbouring reanalysis mid-grid points, for wind class set SB1. To the right the number of incidences of each wind class plotted against wind class number is given.

from the 21 mid-grid points combined. In this way the all points around the region of interest are given equal importance. Figure 19 shows that the behaviour of this wind class set is similar to the more conventional wind classes based on a single locations large scale winds. However the error introduced by the wind class system changes less over the region of interest, Fig 20. compared to the wind class set based on one location, (SB1 in Fig 9). Note the geostrophic winds are slightly different in this case. This is because a factor is not used to adjust the geostrophic wind as a function of latitude. The adjustment is made when mesoscale modelling is used, in the conventional way, Frank (2001). However in this study, see later chapters, the wind classes are used to apply weights to mesoscale model simulations using WRF. In this case an adjustment based on latitude is not required. In any case the geostrophic winds are the same at 55 N.

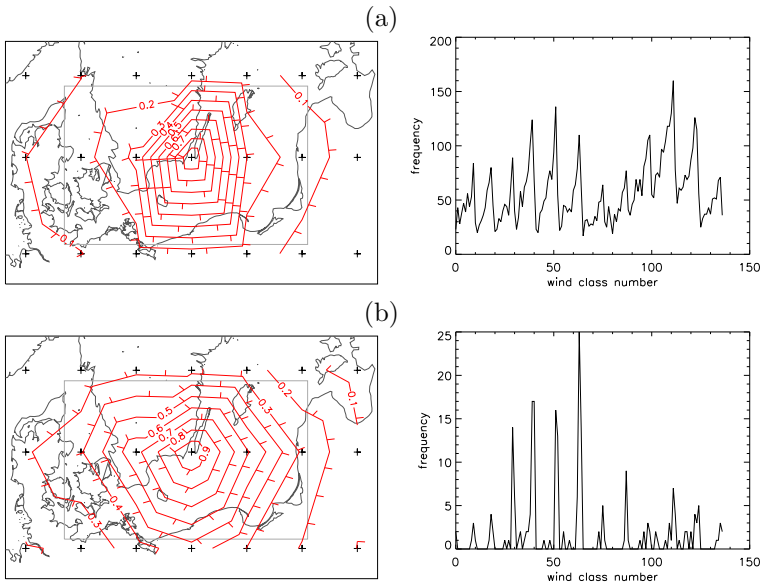

Figure 15: Maps showing the probability of the wind class at 16.25E 56.25N being the same as wind class at neighbouring reanalysis mid-grid points when (a) the wind class is the same for (a) 6 hours and (b) 24 hours, for wind class set SB1. To the right the number of incidences (with consideration to the persistence criterion) of each wind class plotted against wind class number is given.

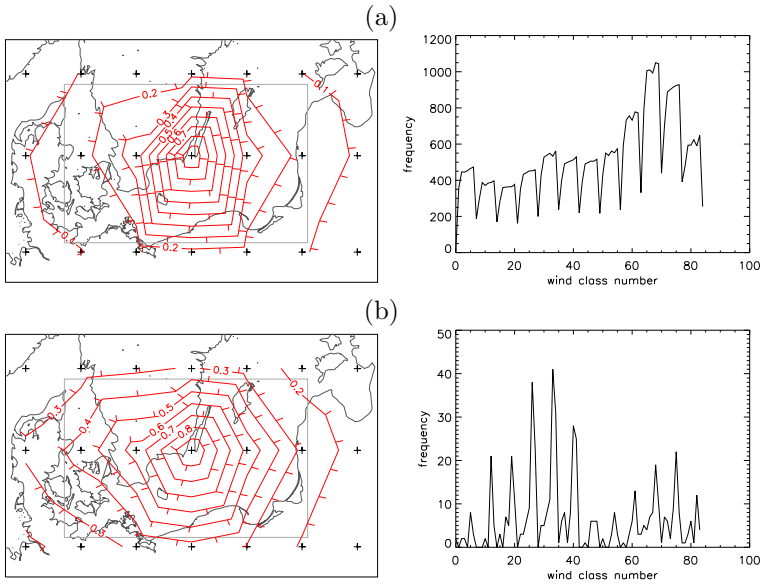

Figure 16: Maps showing the probability of the wind class at 16.25E 56.25N being (a) the same as wind class at neighbouring reanalysis mid-grid points. (b) as in (a) except when the wind class is the same for 24 hours for wind class set SB2. To the right the number of incidences (with consideration to the persistence criterion) of each wind class plotted against wind class number is given.

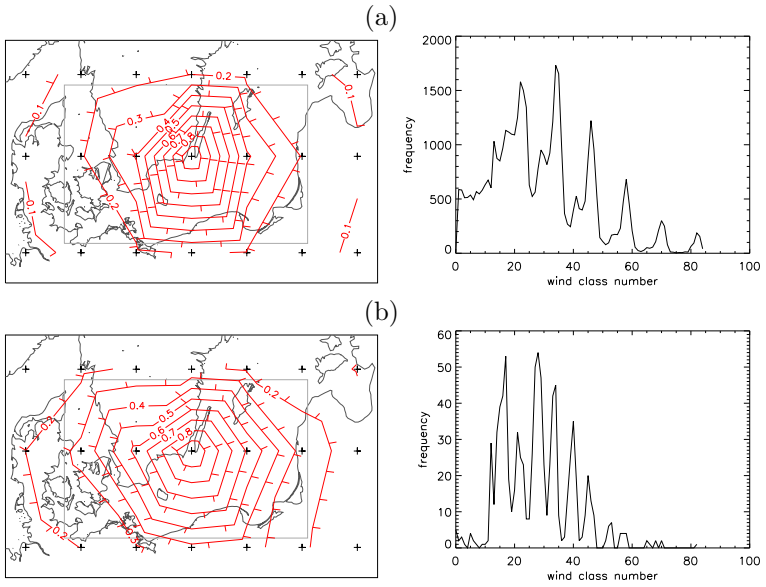

Figure 17: Maps showing the probability of the wind class at 16.25E 56.25N being (a) the same as wind class at neighbouring reanalysis mid-grid points. (b) as in (a) except when the wind class is the same for 24 hours for wind class set SB3. To the right the number of incidences (with consideration to the persistence criterion) of each wind class plotted against wind class number is given.

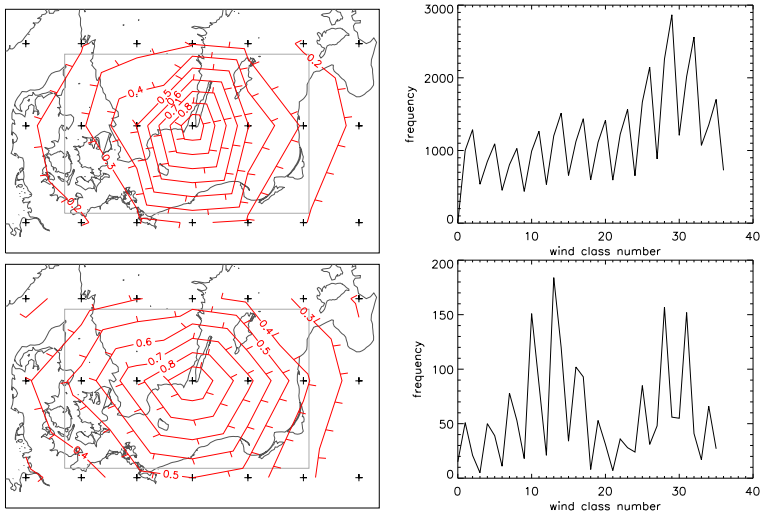

Figure 18: Maps showing the probability of the wind class at 16.25E 56.25N being (a) the same as wind class at neighbouring reanalysis mid-grid points. (b) as in (a) except when the wind class is the same for 24 hours for wind class set SB4. To the right the number of incidences (with consideration to the persistence criterion) of each wind class plotted against wind class number is given.

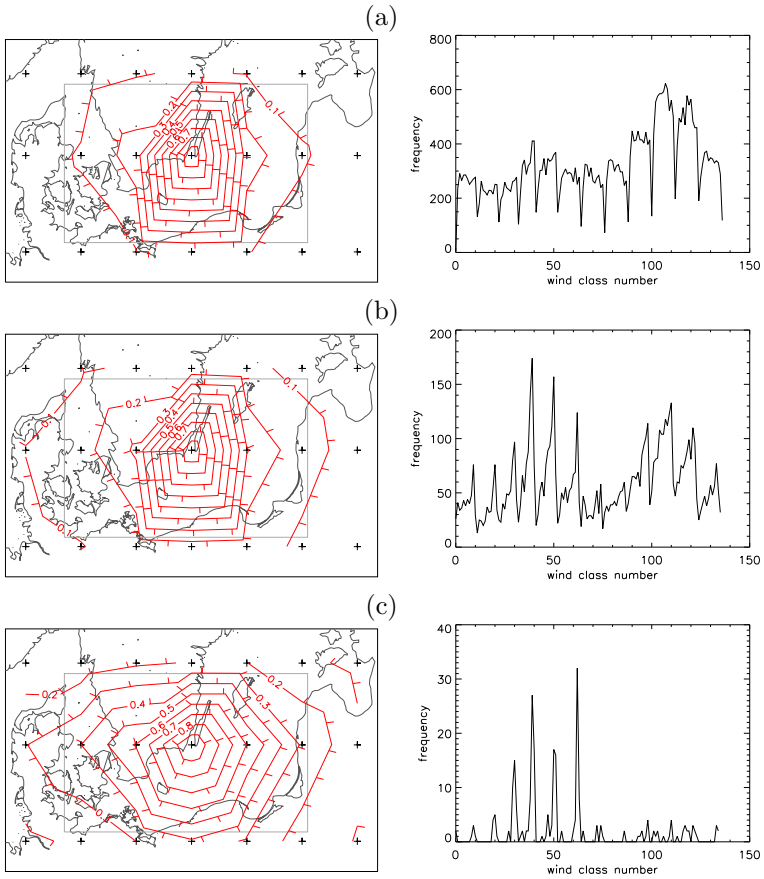

Figure 19: Maps showing the probability of the wind class at 16.25E 56.25N being (a) the same wind class at neighbouring reanalysis mid-grid points. (b) as in (a) except when the wind class is the same for 6 hours and (c) as in (a) except when the wind class is the same for 24 hours for wind class set SB5. To the right the number of incidences (with consideration to the persistence criterion) of each wind class plotted against wind class number is given.

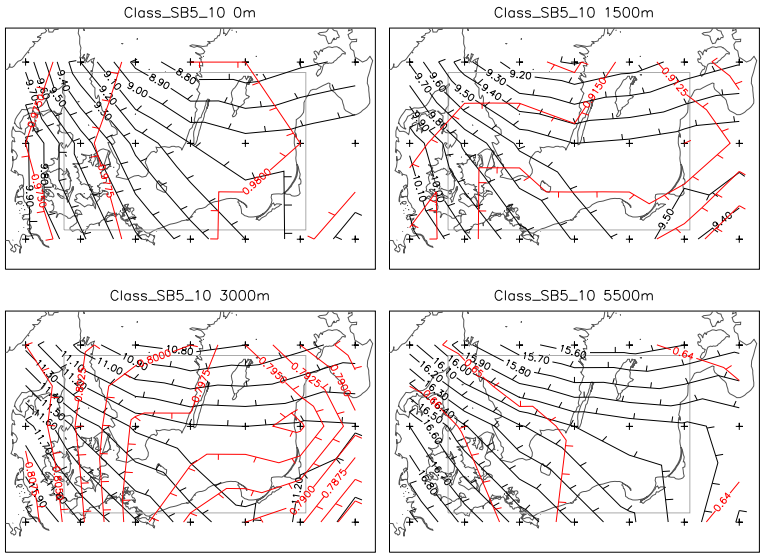

Figure 20: Evaluation of SB5: geostrophic wind speed at sea level as given by NCEP/NCAR reanalysis data 1980–2009 (black contours) and the ratio of the mean of geostrophic wind speed cubed derived from wind classes over that calculated directly for wind class sets (red contours)

5 Validation of WRF model runs against meteorological data

Validation of 4 years of WRF runs (1 January 2007–31 December 2010) is performed at the offshore meteorological masts Fino1 and Fino3 located in the North Sea, Fino2 in the Baltic Sea, wind lidar measurements carried out at the transformer/platform of the Horns Rev II wind farm in the North Sea and an on-land tall meteorological mast at Høvsøre close to the Danish North Sea (see Figure 1). For all locations, the validation is done for:

1. The all-sector mean wind speed profile.
2. The variability in the 1 hour wind speed time series at different heights.
3. The frequency of occurrence of winds in different sectors (wind rose).
4. The direct comparison of observed and WRF-modeled wind speeds.
5. Wind speed distributions.

Finally, a table is presented with performance statistics for the WRF model wind speeds at different heights and locations when compared to the observations.

5.1 Fino1

Fino1 operated during the whole 4 year period of WRF runs so there are more than 25000 hourly samples of paired WRF-observed wind profiles. Figure 21 shows both the all-sector mean wind speed profile from the hourly WRF runs and the observed one. Three model levels are within the observational range 33–100 m and within the mast range, where the cup wind speeds are similarly distorted by the mast structure, i.e. the range between 40 and 90 m[1], both WRF-modeled and observed wind profile agree quite well in both shape and magnitude.

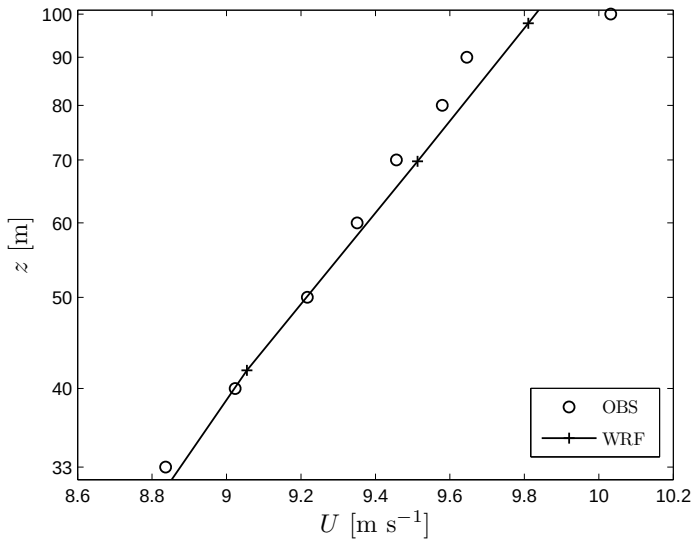

Figure 21: Observed and WRF-modeled all-sector mean wind speed profile at Fino1.

[1]The 33 m level is very close to a helicopter platform and the cup anemometer at 100 m does not have the same mounting on the mast so the distortion is different compared to the lower levels

The WRF model captures the variability of the hourly wind speed as illustrated in Figure 22 well. Here we chose to present a period of 100 days to look properly at the time series but the same results are observed during the 4 year period. Also during these 100 days, episodes of very low (close to 2 m s^{-1}) and very high (close to 25 m s^{-1} at 98 m) wind speeds are observed and the WRF model is able to capture them, although they occur rather drastically.

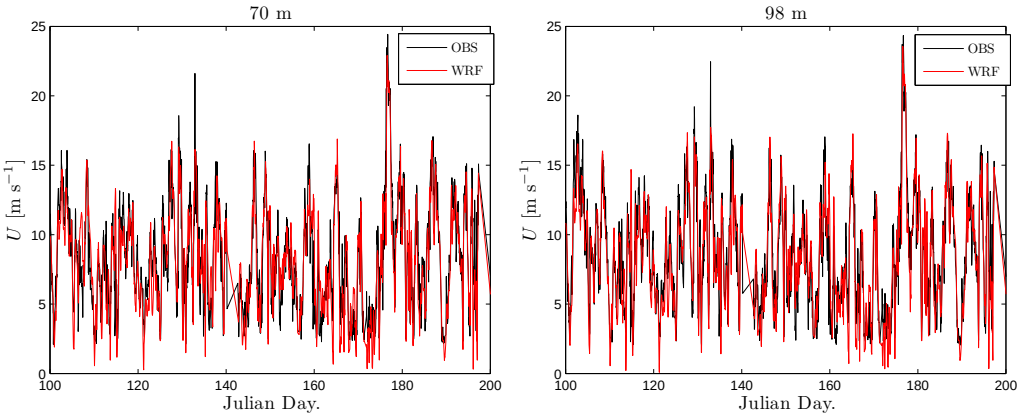

Figure 22: Observed and WRF-modeled hourly wind speed time series at 70 m (left) and 98 m (right) at Fino1.

The WRF model estimates the wind direction very well as seen in Figure 23 compared to the observations and the frequency of occurrence of different wind speed ranges within each sector. The most predominant wind direction, the south-westerly wind, is well predicted and WRF only slightly over-predicts the frequencies on the westerly and north-westerly sectors.

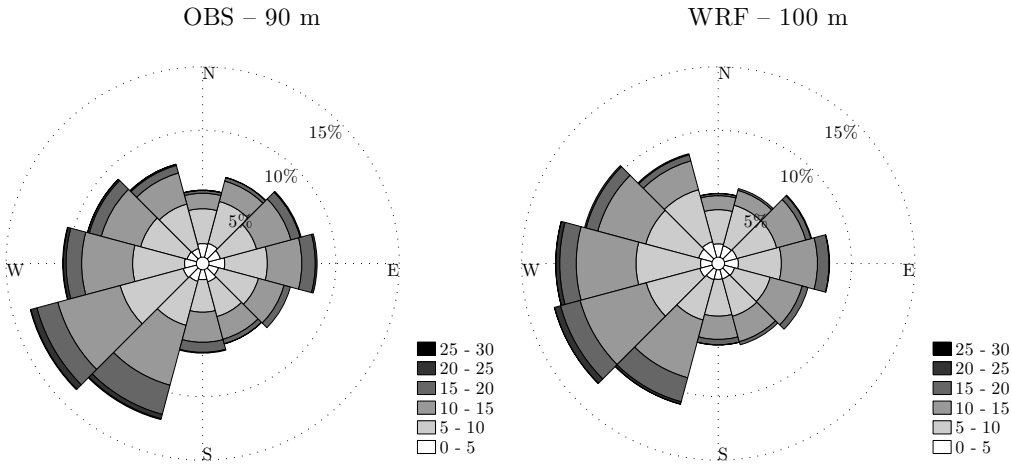

Figure 23: Observed (at 90 m) and WRF-modeled (at 100 m) frequencies of occurrence of winds of different magnitude within sectors (wind roses) at Fino1.

Figure 24 shows the comparison of all hourly wind speeds from the WRF runs at about 98 m and those from the observations at 100 m. WRF wind speeds tend to be 4% lower than the observed wind speeds with a high correlation ($R^2 = 0.81$). However, the WRF mean wind speed is only 2% lower than the observed one at 100 m as seen in Figure 21 and the values shown in Figure 25.

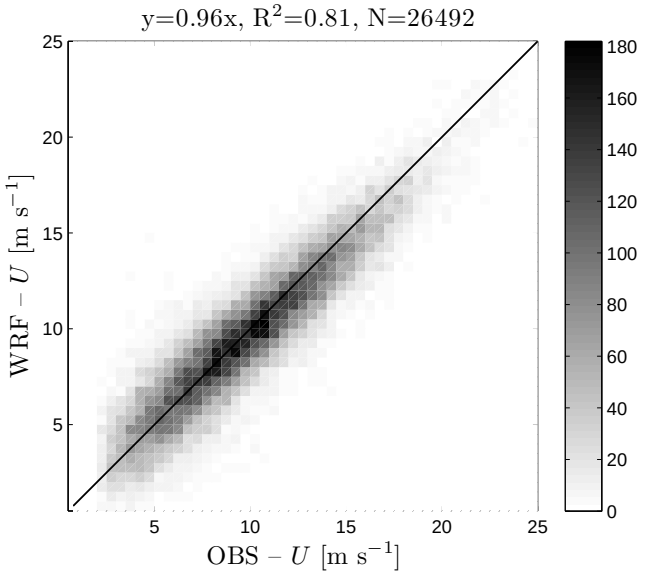

Figure 24: Comparison between all WRF-modeled and observed hourly wind speeds at 100 m at Fino1. Linear regression statistics are given at the frame top.

Wind speed distributions and their Weibull fits for both the WRF and the observed time series at about 100 m are shown in Figure 25. The WRF distribution is more peaky at a value around mean wind speed than the observed one, while the observed wind speed frequencies at high wind speed ranges are higher than the WRF-modeled ones, which in turn estimates a higher observed power density (P/A). However, both distributions and Weibull-fits (including related parameters) are in very good agreement.

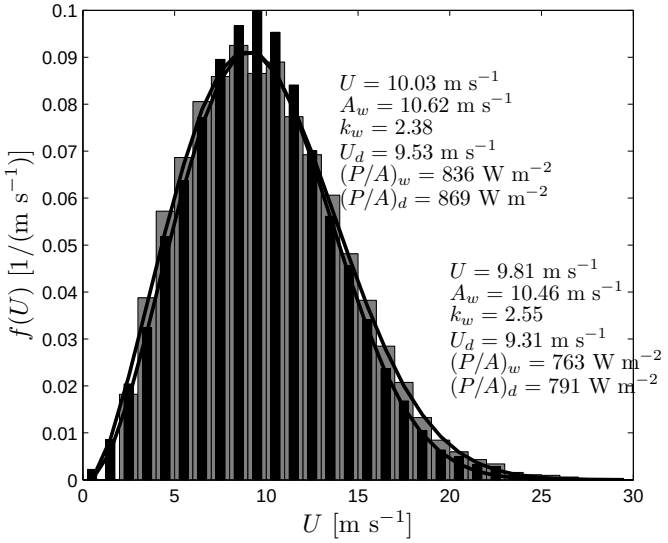

Figure 25: Observed (grey bars) and modeled (black bars) wind speed distributions for the hourly time series at 100 m at Fino1. Weibull fit (solid lines) related parameters are shown with the subindex $_w$ and from the distribution itself with the subindex $_d$ for the observations (top 6 values) and for the WRF model (bottom 6 values).

5.2 Fino2

Fino2 provides valid wind speed measurements starting 16 March 2008 and ending 31 October 2010 so there are about 14000 hourly samples of paired WRF-observed wind

profiles. Figure 26 shows both the all-sector mean wind speed profile from the hourly WRF runs and the observed one. Three model levels are within the observational range 32–102 m and within the mast range, where the cup wind speeds are similarly distorted by the mast structure, i.e. the range between 32 and 90 m[2], both WRF-modeled and observed wind profile agree quite well in terms of shape and there is a slight WRF underprediction of the wind profile at all levels (~ 2 m s^{-1}).

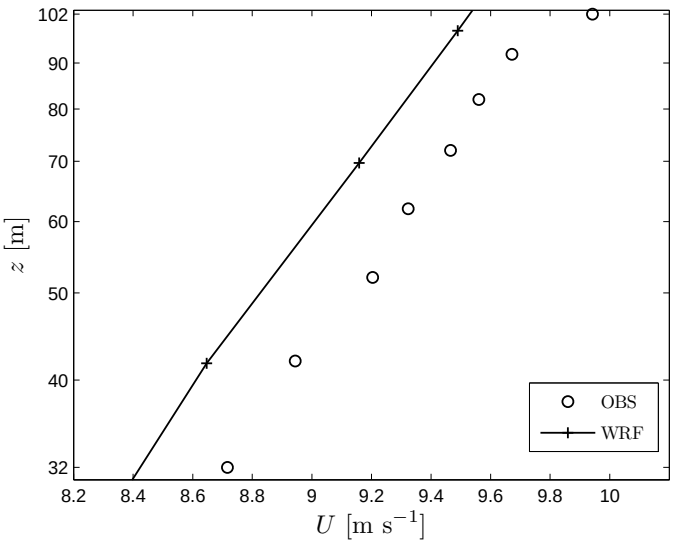

Figure 26: Observed and WRF-modeled all-sector mean wind speed profile at Fino2.

The WRF model captures the variability of the hourly wind speed as illustrated in Figure 27 well. Here we chose to present a period of 100 days to look properly at the time series but the same results are observed during the 2.5 year period. Also during these 100 days, episodes of very low (close to 2 m s^{-1}) and very high (close to 20 m s^{-1}) wind speeds are observed and the WRF model is able to capture them.

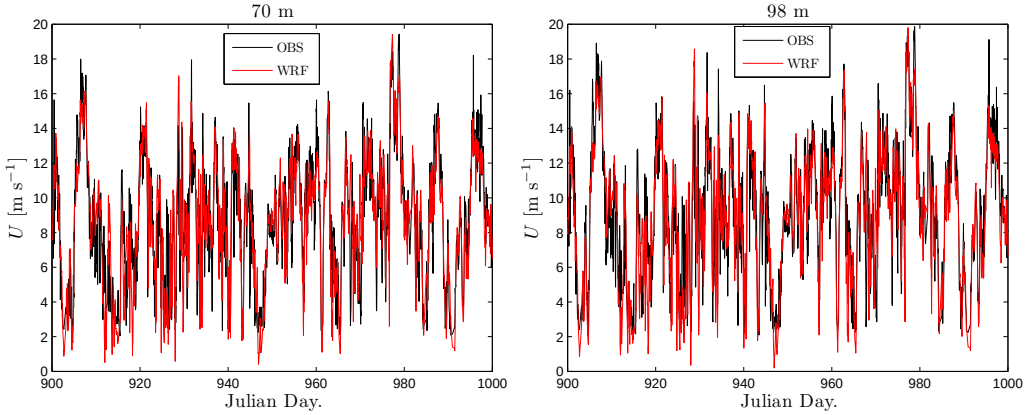

Figure 27: Observed and WRF-modeled hourly wind speed time series at 70 m (left) and 98 m (right) at Fino2.

The WRF model estimates the wind direction very well as seen in Figure 28 compared to the observations and the frequency of occurrence of different wind speed ranges within each sector. The most predominant wind direction, the south-westerly wind, is well predicted and only in the north-easterly directions there is a slight disagreement.

[2]The 32 m level is here included since at Fino2 there is no helicopter platform and the cup anemometer at 102 m does not have the same mounting on the mast so the distortion is different compared to the lower levels

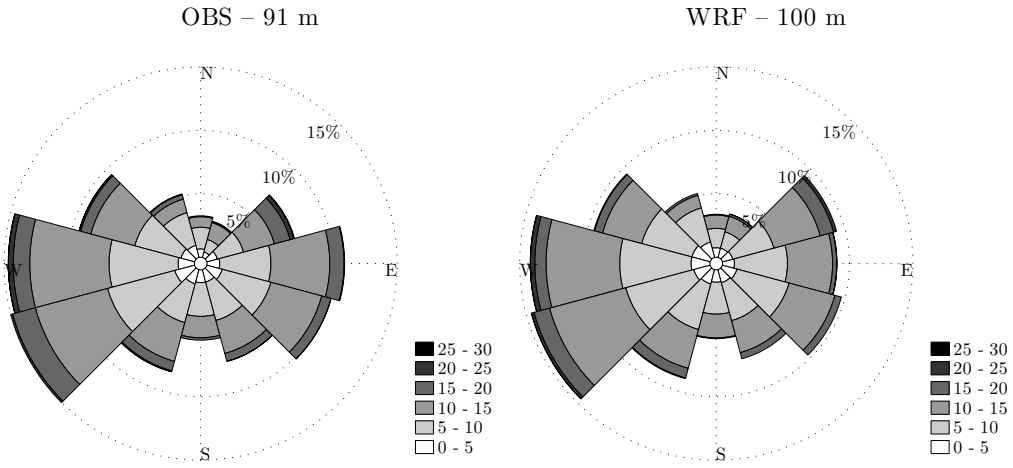

Figure 28: Observed (at 91 m) and WRF-modeled (at 100 m) frequencies of occurrence of winds of different magnitude within sectors (wind rose) at Fino2.

Figure 29 shows the comparison of all hourly wind speeds from the WRF runs at about 98 m and those from the observations at 102 m. WRF wind speeds tend to be 7% lower than the observed wind speeds, but the model and observed heights do not match exactly, explaining partially the increase in WRF wind speed underestimation compared to that found at Fino1. The correlation ($R^2 = 0.76$) is lower than that found at Fino1. However, the WRF mean wind speed is about 4.7% lower than the observed one at 100 m as seen in Figure 26 and the values shown in Figure 30.

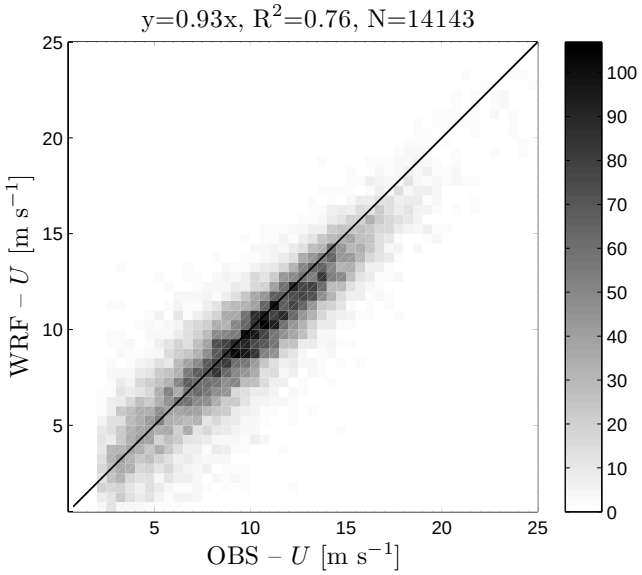

Figure 29: Comparison between all WRF-modeled and observed hourly wind speeds at 100 m at Fino2. Linear regression statistics are given at the frame top.

Wind speed distributions and their Weibull fits for both the WRF and the observed time series at about 100 m are shown in Figure 30. The WRF distribution is also here more peaky at a value around mean wind speed than the observed one, while the observed wind speed frequencies at high wind speed ranges are higher than the WRF-modeled ones, which in turn estimates a higher observed power density. However, both distributions and Weibull-fits (including related parameters) are in very good agreement.

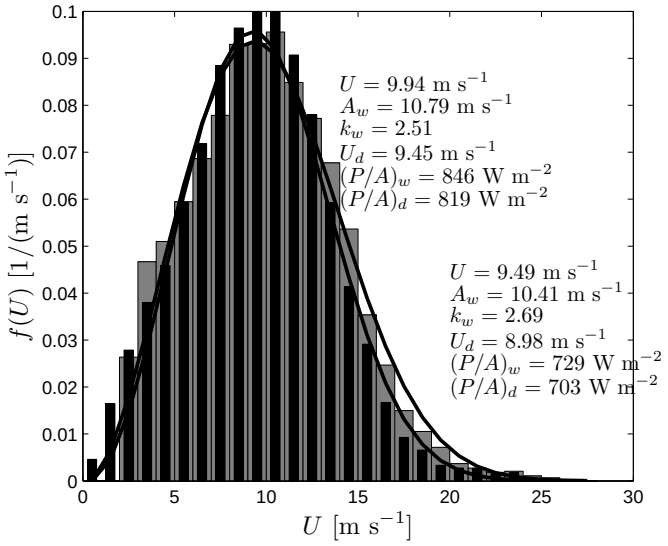

Figure 30: Observed (grey bars) and modeled (black bars) wind speed distributions for the hourly time series at 100 m at Fino2. Weibull fit (solid lines) related parameters are shown with the subindex $_w$ and from the distribution itself with the subindex $_d$ for the observations (top 6 values) and for the WRF model (bottom 6 values).

5.3 Fino3

Fino3 provides valid wind speed measurements starting 5 October 2009 and ending 31 December 2010 so there are about 6500 hourly samples of paired WRF-observed wind profiles. Figure 31 shows both the all-sector mean wind speed profile from the hourly WRF runs and the observed one. Three model levels are within the observational range 30–106 m. Although from the observed wind profile it seems that all levels are mast distorted differently, both WRF-modeled and observed wind profiles agree in terms of shape and, as with the Fino2 observations, there is a slight WRF under-prediction of the wind profile at all levels (~ 2 m s^{-1}).

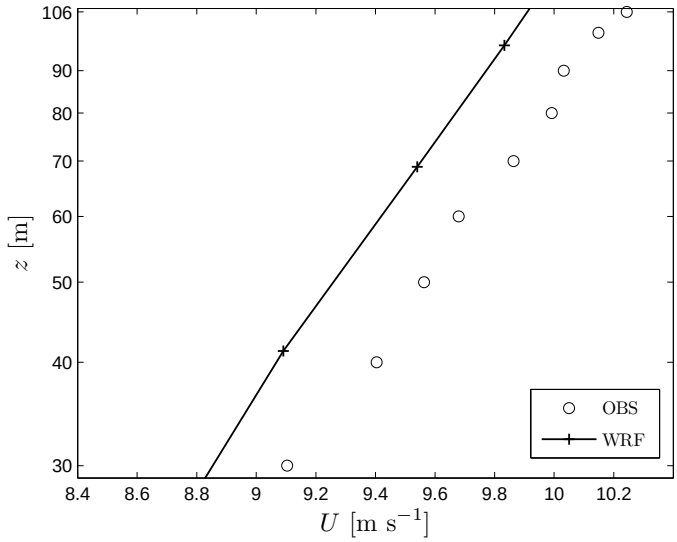

Figure 31: Observed and WRF-modeled all-sector mean wind speed profile at Fino3.

The WRF model also captures the variability of the hourly wind speed as illustrated in Figure 32 well. Here we chose to present a period of 100 days to look properly at the

time series but the same results are observed during the 1 year period. Also during these 100 days, episodes of very low (close to 2 m s^{-1}) and very high (close to 20 m s^{-1}) wind speeds are observed and the WRF model is able to capture them.

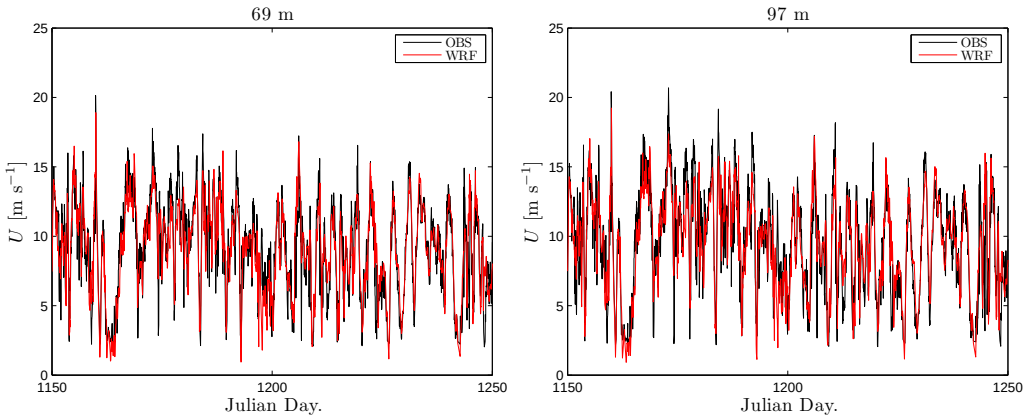

Figure 32: Observed and WRF-modeled hourly wind speed time series at 69 m (left) and 97 m (right) at Fino3.

The WRF model estimates the wind direction very well as seen in Figure 33 compared to the observations and the frequency of occurrence of different wind speed ranges within each sector. The most predominant wind directions, the north-westerly winds, are well predicted and these are the ones showing the largest differences.

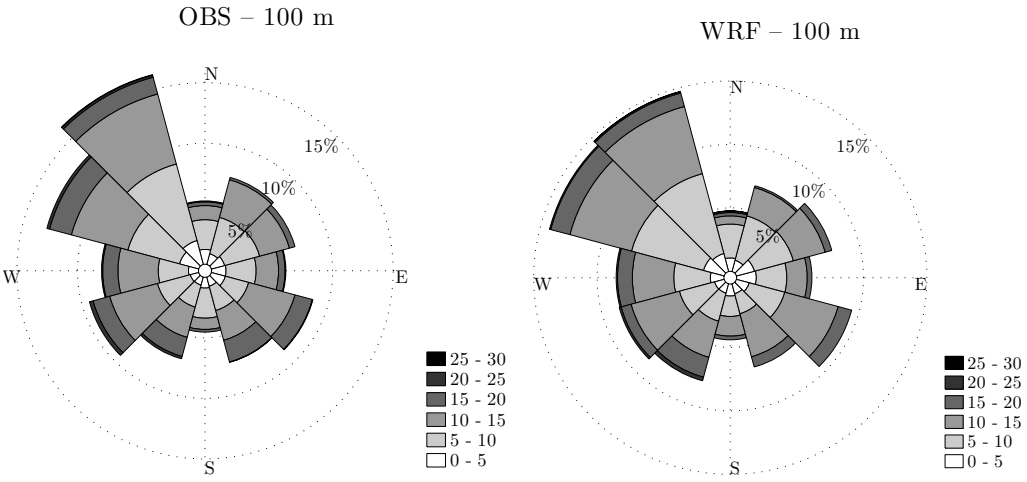

Figure 33: Observed and WRF-modeled frequencies of occurrence of winds of different magnitude within sectors (wind rose) at 100 m at Fino3.

Figure 34 shows the comparison of all hourly wind speeds from the WRF runs at about 97 m and those from the observations at 100 m. WRF wind speeds tend to be 5% lower than the observed wind speeds, somewhere in between the results found at Fino1 and Fino2. The correlation (R^2 = 0.82) is higher than that found at Fino2. However, the WRF mean wind speed is about 3% lower than the observed one at 100 m as seen in Figure 31 and the values shown in Figure 35.

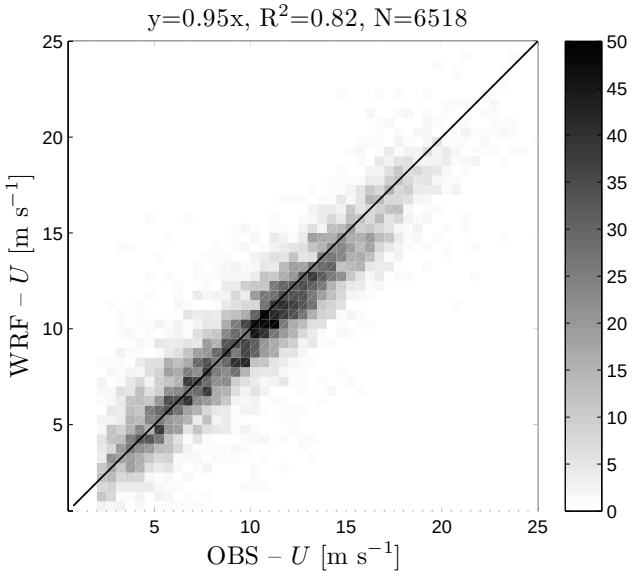

Figure 34: Comparison between all WRF-modeled and observed hourly wind speeds at 100 m at Fino3. Linear regression statistics are given at the frame top.

Wind speed distributions and their Weibull fits for both the WRF and the observed time series at about 100 m are shown in Figure 35. The WRF distribution is not much more peaky compared to the observed one (as found at Fino1 and Fino2), which is translated in a rather similar Weibull-k value. The observed wind speed frequencies at high wind speed ranges are again higher than the WRF-modeled ones, which in turn estimates a higher observed power density. However, both distributions and Weibull-fits (including related parameters) are in very good agreement.

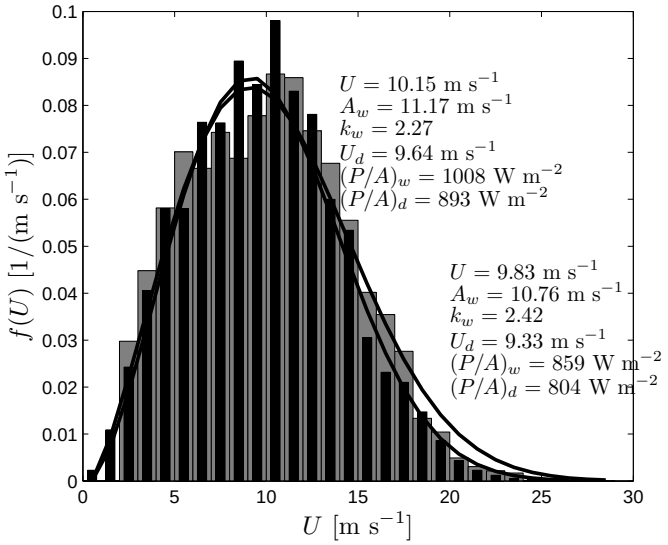

Figure 35: Observed (grey bars) and modeled (black bars) wind speed distributions for the hourly time series at 100 m at Fino3. Weibull fit (solid lines) related parameters are shown with the subindex $_w$ and from the distribution itself with the subindex $_d$ for the observations (top 6 values) and for the WRF model (bottom 6 values).

5.4 Høvsøre

The meteorological mast at Høvsøre, as Fino1, operated during the whole 4 year period of WRF runs so there are almost 28000 hourly samples of paired WRF-observed wind

profiles. Figure 36 shows both the all-sector mean wind speed profile from the hourly WRF runs and the observed one. Five model levels are within the observational range 10–160 m[3], where both WRF-modeled and observed wind profiles agree well in both shape and magnitude.

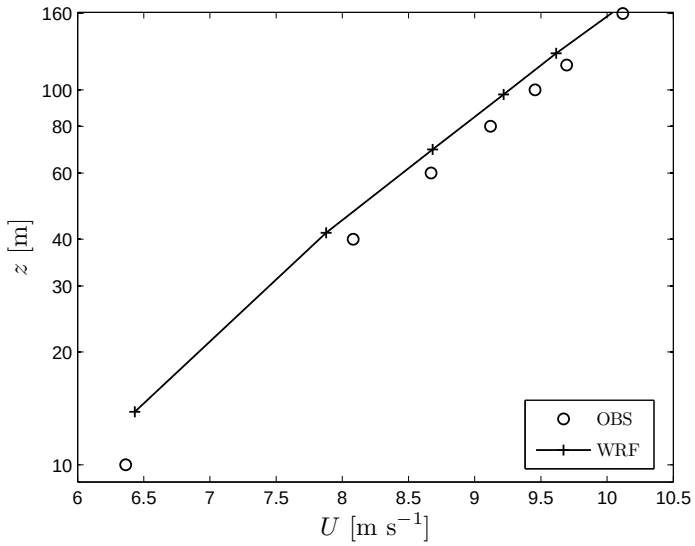

Figure 36: Observed and WRF-modeled all-sector mean wind speed profile at Høvsøre.

The WRF model also captures the variability of the hourly wind speed as illustrated in Figure 37 well. Here we chose to present a period of 100 days to look properly at the time series but the same results are observed during the 4 year period. Also during these 100 days, episodes of very low (close to 1 m s^{-1}) and very high (close to 25 m s^{-1} at 97 m) wind speeds are observed and the WRF model is able to capture them well.

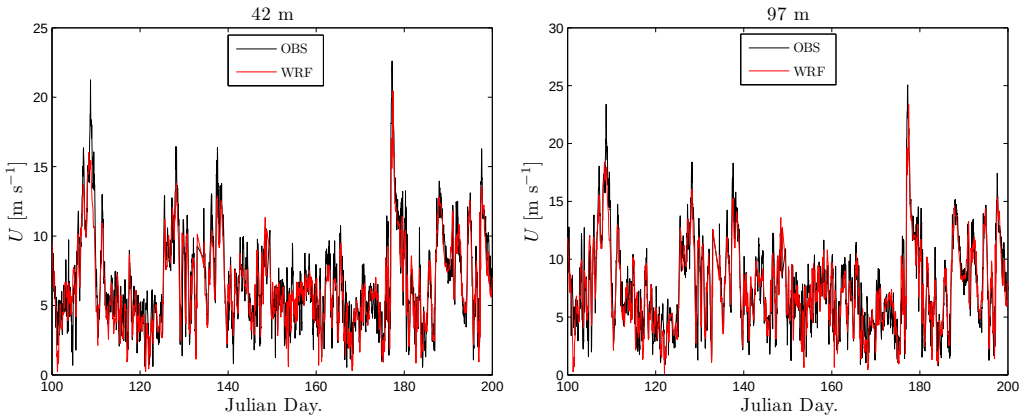

Figure 37: Observed and WRF-modeled hourly wind speed time series at 42 m (left) and 97 m (right) at Høvsøre.

The WRF model estimates the wind direction well as seen in Figure 38 compared to the observations and the frequency of occurrence of different wind speed ranges within each sector. There are few appearances of wind speeds above 30 m s^{-1} in the observations not simulated by WRF. The most predominant wind direction, the north-westerly wind, is well predicted and WRF only slightly over-predicts the frequencies on the westerly and south-westerly sectors.

[3]A model level at 10 m is also available but for the final boundary-layer parametrization, this level is diagnosed not prognosticated, and the results do not agree with the wind speed at higher levels

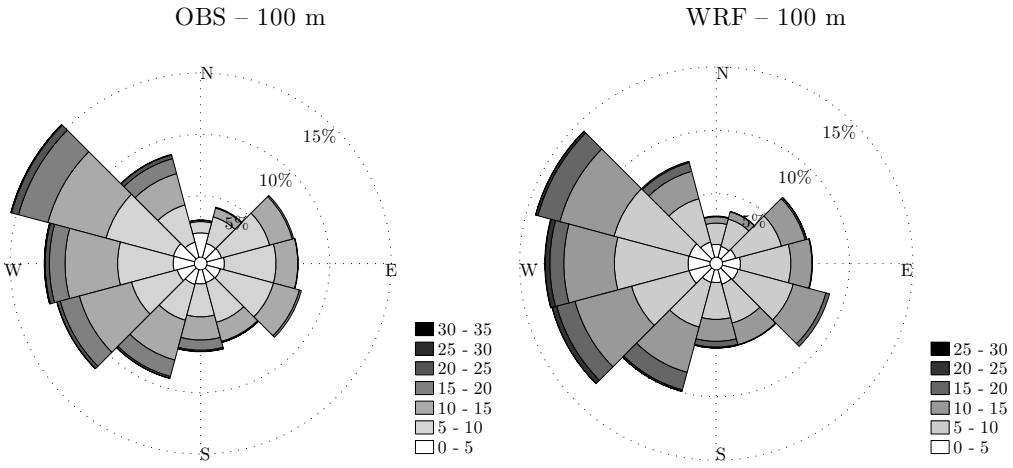

Figure 38: Observed and WRF-modeled frequencies of occurrence of winds of different magnitude within sectors (wind rose) at 100 m at Høvsøre.

Figure 39 shows the comparison of all hourly wind speeds from the WRF runs at about 97 m and those from the observations at 100 m. WRF wind speeds, also for this land location, tend to be 6% lower than the observed wind speeds with a high correlation ($R^2 = 0.82$ which is the same as that found in Fino3). However, the WRF mean wind speed is only 2.5% lower than the observed one at 100 m as seen in Figure 36 and the values shown in Figure 40.

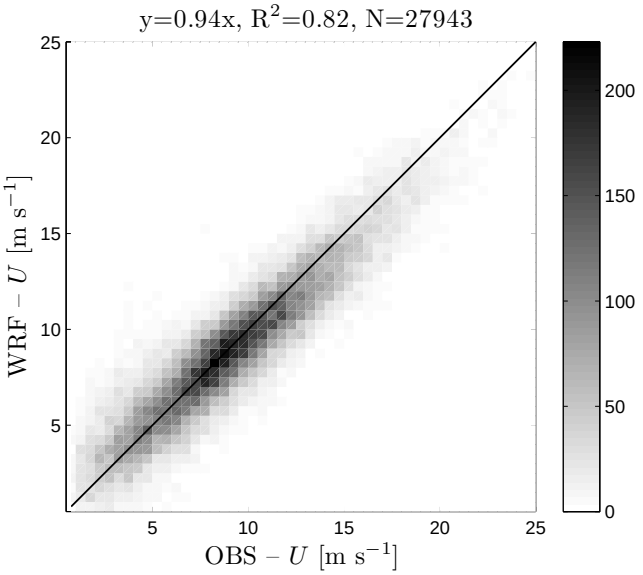

Figure 39: Comparison between all WRF-modeled and observed hourly wind speeds at 100 m at Høvsøre. Linear regression statistics are given at the frame top.

Wind speed distributions and their Weibull fits for both the WRF and the observed time series at about 100 m are shown in Figure 40. The WRF distribution is again more peaky compared to the observed one (as found at Fino1 and Fino2). The observed wind speed frequencies at high wind speed ranges are also higher than the WRF-modeled ones, which in turn estimates a higher observed power density. However, both distributions and Weibull-fits (including related parameters) are in good agreement.

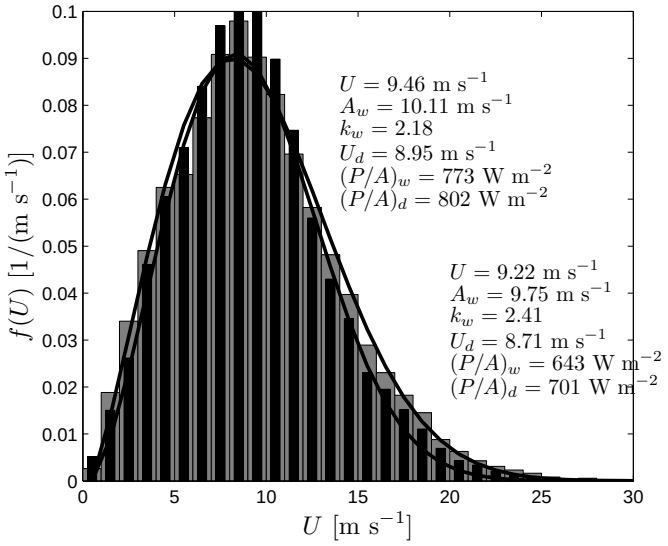

Figure 40: Observed (grey bars) and modeled (black bars) wind speed distributions for the hourly time series at 100 m at Høvsøre. Weibull fit (solid lines) related parameters are shown with the subindex $_w$ and from the distribution itself with the subindex $_d$ for the observations (top 6 values) and for the WRF model (bottom 6 values).

5.5 Horns Rev II

At the platform/transformer of the offshore wind farm Horns Rev II, a wind lidar is installed and provided valid wind speed measurements starting 25 June 2009 and ending 31 December 2010 so there are about 6800 hourly samples of paired WRF-observed wind profiles. Figure 41 shows both the all-sector mean wind speed profile from the hourly WRF runs and the observed one. Four model levels are within the observational range 66–286 m. Although from the observed wind profile the wake of the wind farm has a clear impact on the wind speed, particularly below 200 m, it seems that both observed and WRF-modeled wind speeds asymptotically approach well at the higher levels, where the wind speed is over-predicted by WRF only 0.05 m s^{-1}.

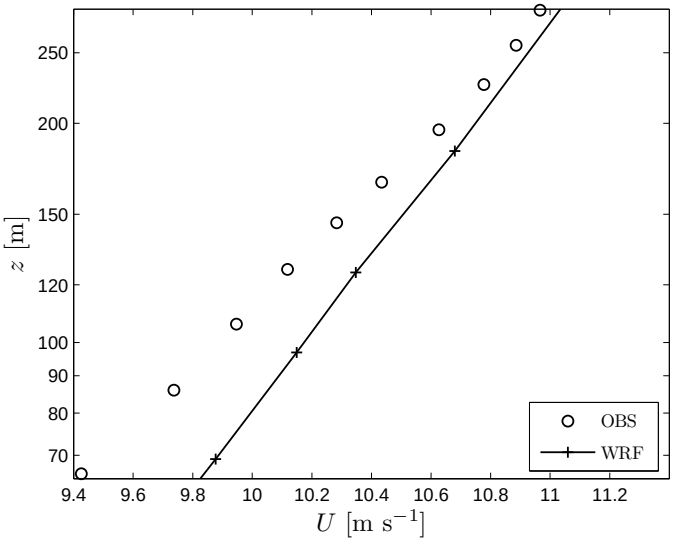

Figure 41: Observed and WRF-modeled all-sector mean wind speed profile at Horns Rev II.

The WRF model also captures the variability of the hourly wind speed at the high observational levels at Horns Rev II ($\sim$ 125 and $\sim$ 299 m) as illustrated in Figure 42 well. Here we chose to present a period of 100 days to look properly at the time series but the same results are observed during the 1.5 year period. Also during these 100 days, episodes of very low (close to 1 m s^{-1}) and very high (close to 30 m s^{-1}) wind speeds are observed and the WRF model is able to capture them well.

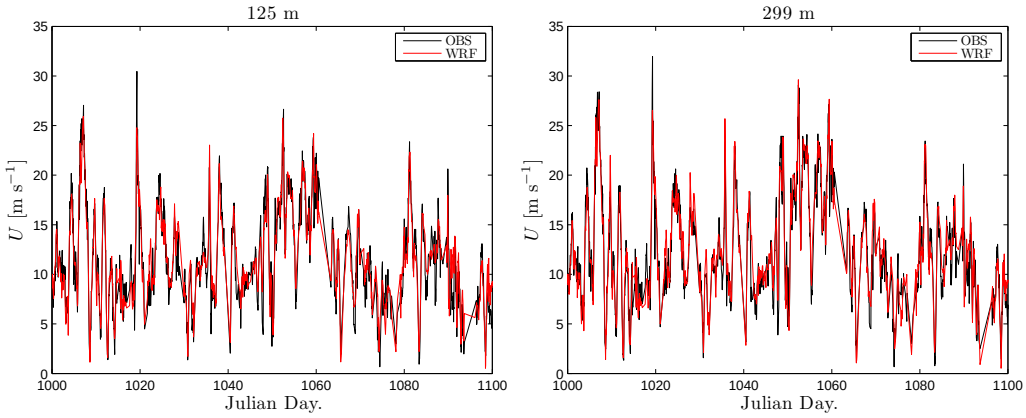

Figure 42: Observed and WRF-modeled hourly wind speed time series at 125 m (left) and 299 m (right) at Horns Rev II.

The WRF model estimates the wind direction well as seen in Figure 43 compared to the observations and the frequency of occurrence of different wind speed ranges within each sector. The largest differences are observed in the most predominant wind directions (westerlies), but observations on these sectors are directly affected by the wind farm.

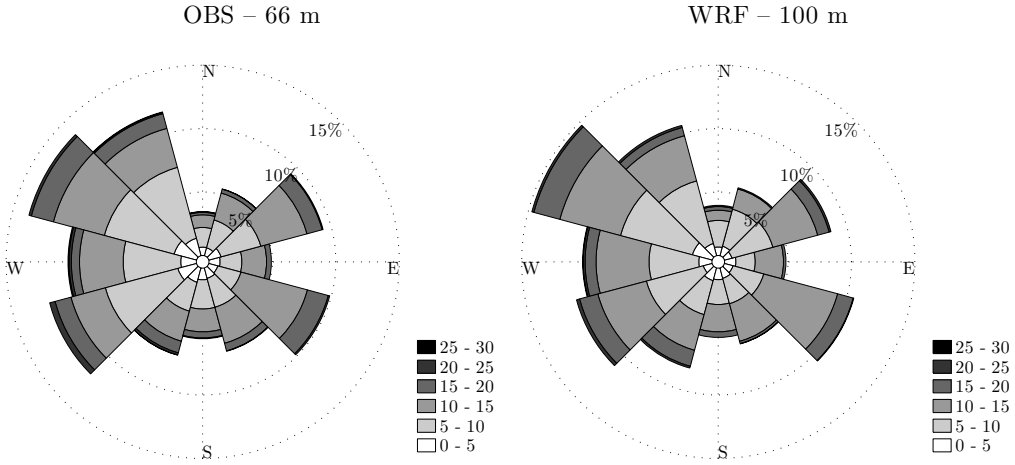

Figure 43: Observed (at 66 m) and WRF-modeled (at 100 m) frequencies of occurrence of winds of different magnitude within sectors (wind rose) at Horns Rev II.

Figure 44 shows the comparison of all hourly wind speeds from the WRF runs at about 97 m and those from the observations interpolated at 100 m. WRF wind speeds tend to be only 1% lower than the observed wind speeds with the highest correlation found from this validation ($R^2 = 0.83$). However, the WRF mean wind speed is 2.7% higher than the observed one at 100 m as seen in Figure 41 and the values shown in Figure 45.

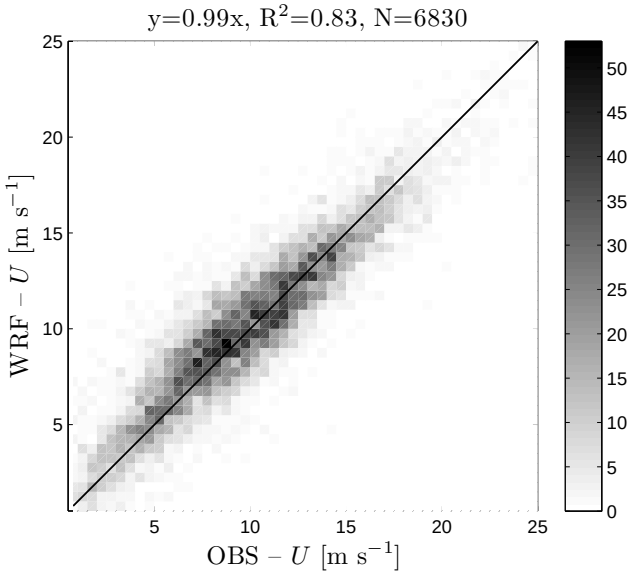

Figure 44: Comparison between all WRF-modeled and observed hourly wind speeds at 100 m at Horns Rev II. Linear regression statistics are given at the frame top.

Wind speed distributions and their Weibull fits for both the WRF and the observed time series at about 100 m are shown in Figure 45. The WRF distribution is once again more peaky compared to the observed one (as found at Fino1, Fino2 and Høvsøre). The observed wind speed frequencies at high wind speed ranges are nevertheless nearly the same as those WRF-modeled, so the estimates of power density are very close. Both distributions and Weibull-fits (including related parameters) are in very good agreement.

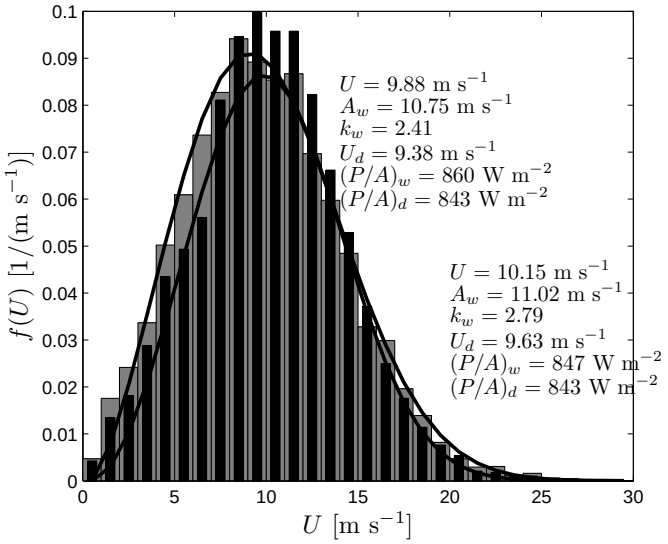

Figure 45: Observed (grey bars) and modeled (black bars) wind speed distributions for the hourly time series at 100 m at Horns Rev II. Weibull fit (solid lines) related parameters are shown with the subindex $_w$ and from the distribution itself with the subindex $_d$ for the observations (top 6 values) and for the WRF model (bottom 6 values).

5.6 WRF overall performance

Final performance statistics for the WRF model wind speeds at different heights and locations when compared to the observations are presented in Table 4. It is found that

the RMSE between the observed and the modeled wind speeds is close to 2 m s^{-1} and that the WRF model does not show a clear improvement in performance when evaluated in an specific area, height level or for a larger number of samples.

Table 4: RMSE in m s^{-1} between the observation and the WRF model wind speeds for different heights and locations. In parenthesis the number of 1 hour samples used for the statistics.

Height	Fino 1 (26492)	Fino 2 (14143)	Fino 3 (6518)	Høvsøre (27943)	Horns Rev II (6830)
40 m	1.89	1.88	1.64	1.69	-
70 m	2.06	2.02	1.74	1.88	1.75
100 m	1.86	2.06	1.82	-	1.77
183 m	-	-	-	-	1.74

6 QuickSCAT

6.1 Introduction

Satellite observations of wind over the ocean offer high spatial and temporal resolution. Spaceborne instruments have been designed and launched in orbit during the last thirty years. Especially, scatterometers have provided long records of accurate wind speed and direction observations.

Their principle of function is based on measuring the incoming microwave radiation backscattered from the sea surface due to small scale waves, assumed to be in equilibrium with the wind. Empirical algorithms, the Geophysical Model Functions (GMF) are applied to the radar backscatter, observed from multiple viewing angles, in order to obtain wind information. The physical product is the Equivalent Neutral Wind (ENW) at 10 m above sea surface, following the definition of Liu and Tang (1996).

Parameters known to have an impact on the accuracy of retrieved information include rain, sea temperature, salinity, contaminants, large swell waves or rapidly varying winds and the atmospheric stability. Especially rain, changes the usual ocean surface and attenuates and scatters the radar energy at 13.4 GHz (Hoffman and Leidner, 2005). A descriptive overview of the progress in scatterometer application can be found in Liu (2002).

Atmospheric stratification is not always neutral, thus ENW may differ from the actual wind at the height of 10 m but usually this difference is not larger than 0.5 m s^{-1} (M. A. Bourassa and Smith, 2003). Recently, A.B. Kara and Pauley (2009) found that the impact of air-sea stratification can give rise to monthly mean differences larger than 0.5 m s^{-1} in some regions of the Mediterranean Sea, but generally did not exceed 0.2 m s^{-1} over the majority of the basin.

NASA's QuikSCAT mission was launched in July 1999 and until November 2009 it recorded information about wind speed and direction over the ocean surface. At a height of approximately 800 km, completing each orbit in 100 minutes and observing a wide swath of 1800 km, it provided near-global coverage of the ocean surface twice every day. Data are available from different processing and distribution centres. An extensive list of distributors can be found in the Physical Oceanography Distributed Active Archive Center (PO.DAAC).

QuikSCAT observations have been validated against in situ measurements from buoys, meteorological masts and research vessels. N. Ebuchi and Caruso (2002) found an RMSE difference of 1 m s^{-1} for speed and 20^o for direction, when measurements higher than 3 m s^{-1} were used. M. A. Bourassa and Smith (2003); M.H. Pickett and Wash (2003); W. Tang and Stiles (2004); K. Satheesan and Kuroda (2007); J. Boutin and Piolle (2009); S. Pensieri and Schiano (2010); B.R. Furevik (2010) evaluated QuikSCAT against in situ observations in the open ocean and coastal areas at different locations. J. Winterfeldt and Weisse (2010) compared QuikSCAT Level2B products with buoy wind speed in the eastern North Atlantic and the North Sea while Kolstad (2008) derived a climatology for the Nordic Seas using eight years of QuikSCAT data.

Mean spatial wind characteristics and the climatology of certain regions or the global ocean using QuikSCAT have been investigated by Risien and Chelton (2006) and Zecchetto and Biasio (2007). Comparisons between QuikSCAT and NWP models were performed by Chelton and Freilich (2005), D.B. Chelton and Ahn (2006) and C. Accadia and Speranza (2007).

Here, we used 10 years of QuikSCAT observations to study the long-term wind characteristics of the South Baltic Sea. The purpose is to use these results for comparisons against other spaceborne instruments, such as the Synthetic Aperture Radar (SAR) and numerical model results from WRF, in order to obtain a multi-source description of the average wind regime in the region.

A description of the satellite data and the methods applied can be found in Section 6.2. Results are presented, as seasonal and long-term values, in Section 6.3. A discussion and the main conclusions can be found in Section 6.4.

6.2 Data and Methods

QuikSCAT Data

QuikSCAT gridded data were obtained from Remote Sensing Systems (RSS). They were produced daily by mapping the scatterometer orbital data to a 0.25 deg longitude by 0.25 deg latitude Earth grid. For the domain of interest the grid cell size was approximately 16.83 km by 27.82 km. Overpass time was around 06:00 and 18:00 UTC, thus capturing early morning and evening conditions.

Due to the scatterometer's principle of function, no wind information can be obtained over sea ice. Moreover, scatterometers have a sensitivity to rain. Thus, RSS used contemporaneous microwave radiometer measurements for sea ice and rain detection. Due to the ambiguity applied to the wind retrieval in the presence of rain, all relevant flags were utilized and quality control demanded that all flags show no rain for an observation to be included in the processing. To the contrary, there was no control over the sea ice mask as there was no relevant flag included in the data set.

WRF Model Outputs

Outputs from the WRF (Weather Research and Forecasting) mesoscale model, were produced from December, 31st 2006 to October, 31st 2009. The WRF 10 m winds were created by simple extrapolation (cubic splines under tension) of the model levels above at 14, 42, 70 and 98 m. No attempt was made to convert them to neutral.

For comparisons against QuikSCAT, the time collocated model outputs were selected for every day of the evaluation period. A satellite retrieval was used only if it was flagged as rain free by both the scatterometer and the collocated radiometer.

Methods

General wind characteristics were calculated for the period November 1999 to October 2009. The seasonal distribution was estimated following the conventional separation of months, i.e. S-O-N as autumn, D-J-F as winter, M-A-M as spring and J-J-A as summer.

Each season, defined as a 3-month period had an average of 91 days, thus 182 passes. For the 10-year period, this corresponded to maximum amount of 1820 passes per season. Only grid cells with at least 180 rain free observations, corresponding to two rain free observations daily for a season, were included in the processing.

Average wind characteristics were calculated for the same period, irrespective of season. Only grid cells with at least 730 rain free observations, were included in the processing.

Wind Statistics The frequency distribution of wind speed, $f(u)$, is represented by the Weibull distribution (Troen and Petersen, 1989), expressed in Eq. 1. The scale parameter A is associated with the mean wind. The shape parameter k describes the spread of the distribution,

$$f(u) = \frac{k}{A}\left(\frac{u}{A}\right)^{k-1} \exp\left(-\left(\frac{u}{A}\right)^{k}\right). \quad (1)$$

From the Weibull A and k parameters, using the gamma function Γ and the density of air ρ ($\sim$1.245 g m^{-3} at 10°C), one can estimate the available wind power density E (Eq. 2).

$$E = \frac{1}{2}\rho A^3 \Gamma \left(1 + \frac{3}{k}\right). \quad (2)$$

6.3 Results

Seasonal Variation Seasonal data availability and mean wind are shown in Figure 46. Given the fact that not all passes were available or not all observations occurred under rain-free conditions, a maximum of 1757 rain-free observations for the autumn season was observed while the lowest of maxima, 1742 measurements, occurred during winter.

Most part of the South Baltic region was not observed during winter and early spring due to the sea ice flag. Maximum area coverage was observed for summer and autumn. Only the central part of the Baltic Sea was well observed during the year. Results for the south part will be biased towards summer and autumn conditions.

Mean wind speed ranged from 5 m s^{-1} for spring and summer, to 8.5 m s^{-1} in autumn and 9-9.5 m s^{-1} in winter. A noticeable difference between the South Baltic and the eastern North Sea was observed, with higher speeds occurring in the North Sea. Even within the same season, an average difference of 1.5-2 m s^{-1} was observed. Higher winds were observed in the Kattegat Strait, when compared to the South Baltic, especially in spring and summer.

The Weibull A and k parameters are shown in Figure 47. The seasonal variation, as expected, indicated higher values during winter which decreased in spring and summer and started increasing in autumn. The spatial variability of the A parameter was relatively low, with large areas exhibiting similar values. Once again, higher values were observed for the North Sea and for Kattegat and eastern Øresund, when compared to the Baltic Sea.

For the shape parameter k, higher values are generally associated with narrower distributions with a clearly defined, dominant peak. A significant spatial variability was revealed even within the same season. Higher values were observed for in the western part of the basin, especially for summer and autumn. This may have been the case for winter and spring as well, but the lack of data availability due to the sea ice mask caused the lack of information during these periods. In general, lowest values were observed during spring. The spatial variability of the k parameter was higher when compared with the one of the A parameter.

Mean Characteristics A synoptic representation of the different variables shown previously, is presented in Figure 48. Data availability for a given grid cell, reached a maximum of 6774 observations for the 10 years QuikSCAT records. Mean wind speed was 7.5 m $s^{-}1$, for the central part of the Baltic Sea. The standard deviation of the mean wind was found relatively high, ranging from 3.8 m $s^{-}1$ to 4 m $s^{-}1$, again for the central part of the basin where all seasons were well captured. Weibull A ranged between 8.2 m $s^{-}1$ and 8.4 m $s^{-}1$, while the k parameter was around 2.

Wind power density was estimated using the calculated Weibull A and k parameters, for grid cells with more than 730 observations. The low values found in the south-west part of the basin may be attributed to lower data availability, representative of calm conditions. The central region of the Baltic Sea had an average of 400 to 550 W m^{-2}. Significantly higher values were estimated for the eastern North Sea, were 10-year averages reached 700 W m^{-2}.

Comparisons with the WRF Model For the period of investigation, the maximum number of rain-free QuikSCAT retrievals available for comparisons with WRF reached 2027, recorded in the central part of the Baltic Sea and the eastern North Sea. The mean bias shown in Figure 49b, was defined as QuikSCAT minus WRF. For most grid cells, the bias was zero. It was found in favour of WRF, by 0.2 m s^{-1}, for a small area in the

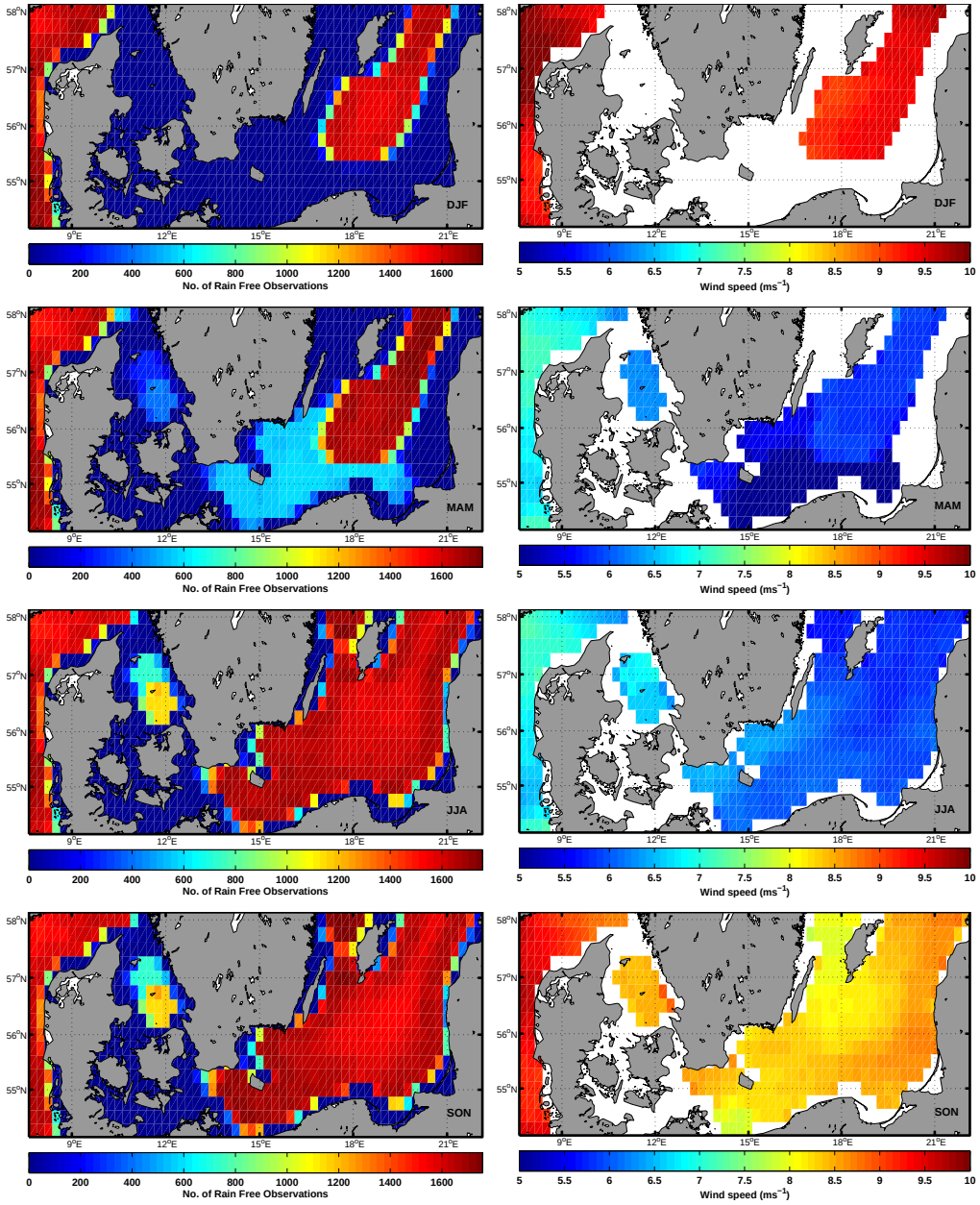

Figure 46: Amount of rain free observations (left) and mean wind speed (right) for every season.

centre of the Baltic basin. Higher biases in favour of QuikSCAT, generally not exceeding 0.4 m s^{-1}, were observed in coastal areas, usually for the first QuikSCAT water grid cell after the land mask.

Standard deviation was on average between 1.4 m s^{-1} and 1.6 m s^{-1}, for the greatest part of the domain. Coastal areas exhibited higher values, reaching up to 2.2 m s^{-1}. Very high values, up to 3 m s^{-1}, were observed in the south-west coast of Norway. This was likely due to the boundary layer scheme used by the model.

The correlation, R^2, between satellite observations and model outputs, reached maximum values of 0.9 for the central part of the Baltic Sea and the eastern North Sea. Lower correlation was observed in areas of higher mean biases and standard deviations. The RMSE was minimum for the largest part of the domain, with the lowest values observed for the eastern North Sea.

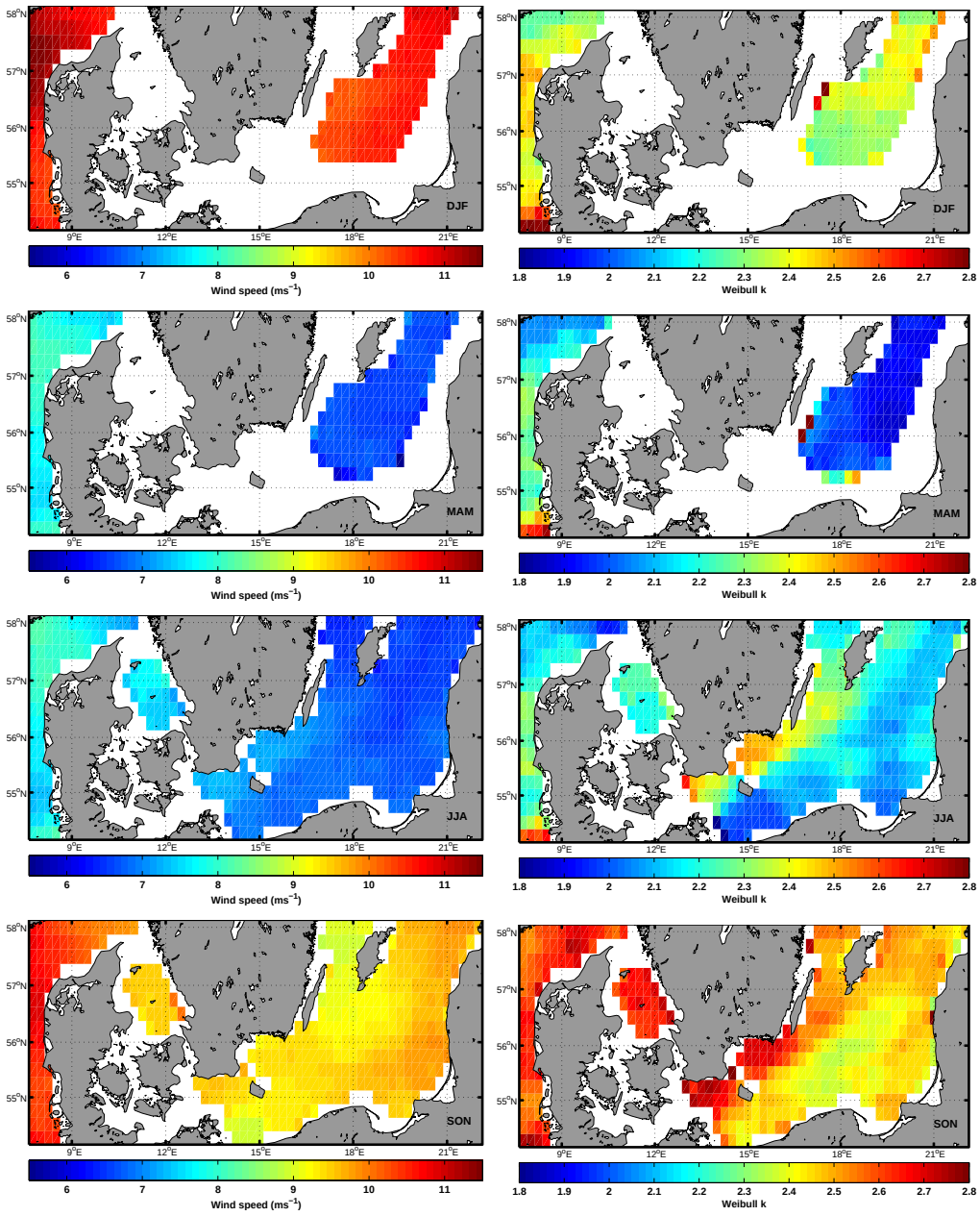

Figure 47: Weibull A (left) and k (right) for every season.

6.4 Discussion and Conclusions

QuikSCAT, with the long period of global ocean wind retrievals, provided a helpful tool for an initial analysis of the wind regime in the South Baltic Sea. Unfortunately, the lack of coverage during winter and early spring in some areas of the domain, will bias results towards summer and autumn conditions. The seasonal variability of wind characteristics, showed a typical decrease of mean speed especially in spring. No particular spatial variability was observed within the same basin, as the wind field was stable for the largest part of the domain. Despite that, a difference between the Baltic Sea and the eastern North Sea was noticeable.

The standard deviation of the mean wind was found high, between 3.8 m s^{-1} and 4.2 m s^{-1}, for the areas with generally high data availability. This can be justified by the fact that such areas were covered throughout the year, thus capturing all varying conditions. Areas with lower data availability were observed mainly during summer and autumn,

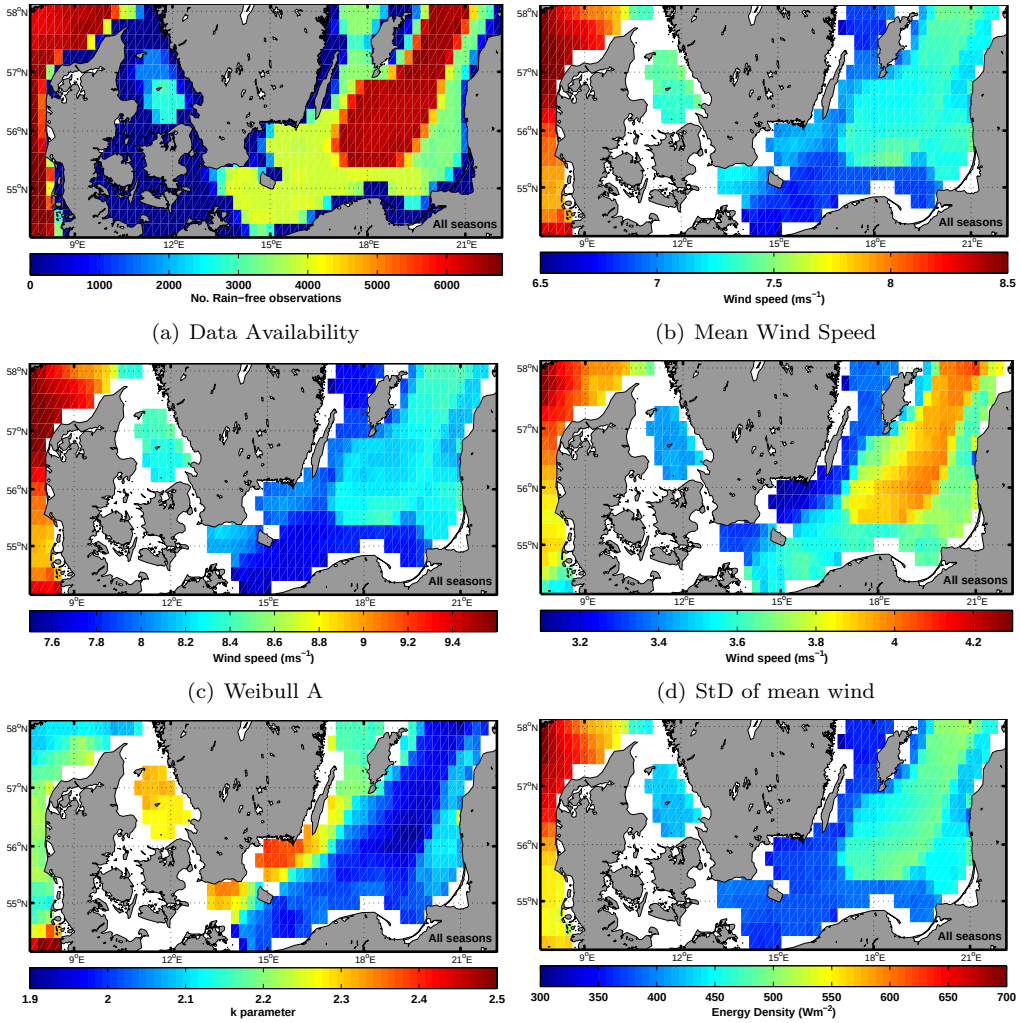

(a) Data Availability

(b) Mean Wind Speed

(c) Weibull A

(d) StD of mean wind

(e) Weibull k

(f) Energy density

Figure 48: Data availability and various wind characteristics for 10 years of QuikSCAT observations.

thus biased towards only low wind conditions, hence the lower standard deviation.

Weibull A and k parameters were in general agreement with other studies. A particularly interesting feature was revealed, regarding the k parameter; high values relative to the surrounding areas were observed in a South-West to North-East direction along Southern Sweden. This may well be connected with the dominant wind direction, which has a similar orientation.

Energy density was found in general lower than in other studies (examples), by an average of 200 W m^{-2}. QuikSCAT provided two observations every day, thus capturing early morning and evening conditions. The time resolution was much different than the standard 10 minute averages of in situ measurements. As the energy density is proportional to the cube of the mean wind, any errors will be significantly magnified.

Comparisons between QuikSCAT wind retrievals and WRF model outputs, indicated very good correlation between satellite observations and model. Mean biases were very low, in the order of 0.2 m s^{-1}, but increased in coastal regions where WRF winds over the seas may be contaminated by winds over land. Given the fact that QuikSCAT refers to the wind under neutral atmospheric stratification and WRF outputs were not corrected according to stability, the current findings are in agreement with results from A.B. Kara and Pauley (2009).

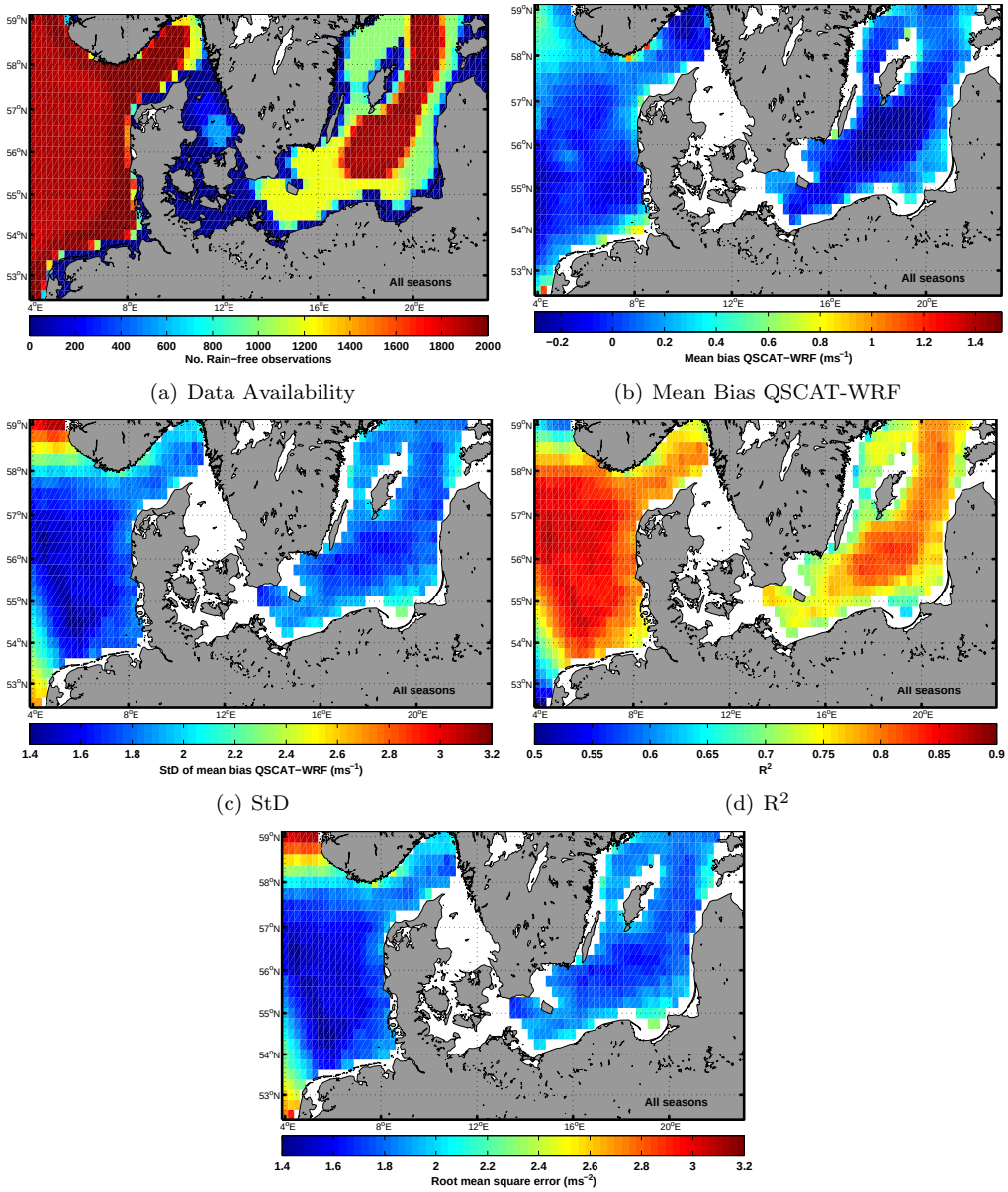

(a) Data Availability

(b) Mean Bias QSCAT-WRF

(c) StD

(d) R^2

(e) RMSE

Figure 49: Error statistics for QuikSCAT-WRF.

It has been shown that satellite wind retrievals can be valuable, complementary to in situ observations. Their high temporal and spatial coverage provides a synoptic representation of real-time conditions, useful for an initial description of the wind regime or validation of mesoscale model outputs.

7 Syntetic Aperture Radar (SAR)

7.1 Introduction

The South Baltic Sea has been mapped by the Advanced SAR (ASAR) on-board the European Space Agency satellite Envisat from 2003 to 2010. Risø DTU collects the radar scenes in near-real-time. Most scenes are from the Wide Swath Mode (WSM). The ocean wind maps are produced in near-real-time using the Johns Hopkins University Applied Physics Laboratory (JHU APL) software ANSWRS (Christiansen et al., 2008; Monaldo, 2000; Monaldo et al., 2003) at Risø DTU. The geophysical model function used is CMOD-5 (Hersbach et al., 2007) in the current project. The wind maps can be viewed at http://www.risoe.dtu.dk/business_relations/Products_Services/Software/VEA_windmaps.aspx

The physical background for SAR being capable of providing offshore winds is the following: capillary waves are generated within seconds by the gustiness of the mean wind. The wind fluctuations appear and decay and similarly do the capillary waves. From this small scale air-sea interaction the surface has a 'roughness'. The rougher the surface, the more efficiently the electromagnetic microwave radiation is scattered in all directions and returned to the radar. Over land and sea ice there are not such processes and SAR cannot map winds over land and sea ice. The geophysical model functions describe mathematically the relationship between the normalized radar cross section (NRCS) and the wind speed at 10 m above sea level, the radar viewing geometry and the actual wind direction. The wind direction is not retrieved from the SAR image but is used as a priori information from the NOGAPS model to initialize the wind retrieval in each grid cell. NOGAPS is the US Navy's Operational Global Atmospheric Prediction System.

The spatial resolution of the ocean wind maps from SAR is set to 1 km by 1 km. Therefore it is possible to observe winds close to the coastline. The imaging takes place in few seconds thus each individual wind map is a snapshot of the offshore winds. More than 1000 wind maps are used in the study. Figures 50–52 show three examples of individual wind maps. Figures. 50 and 52 are from ascending orbits observed around 20.40 UTC while Figure 51 is from descending orbit observed around 09.06 UTC. Envisat orbits Earth in a sun-synchronous polar orbit. This means that a local area is observed at approximately the same time of the day, in the ascending and descending orbits.

The offshore wind map from 12 September 2009 (Figure 50) shows weak winds in most of the area. The arrows indicate the wind direction with westerly flow. The arrows are the NOGAPS global model results, interpolated in time and space to fit best possible the individual SAR fields. The color of the arrow represents the wind speed from NOGAPS. In case this is similar to the SAR wind field, the NOGAPS winds and SAR winds agree very well. Please note the color scale is given both in m s^{-1} and in knots. The direction of the wind can be deduced visually from the SAR image. Wind streaks aligned with the dominant wind direction appear here and there. Also lee effects of land masses and islands are visible. NOGAPS provide wind speed and direction over land and sea. This is in contrast to SAR that only provides winds offshore.

On 28 September 2009 the Envisat ASAR mapped a 2000 km long track from Poland to the Gulf of Bothnia in the north, see Figure 51. The ocean winds show two distinct weather conditions with strong winds in the north and south and with weaker winds in the central part. Winds are from westerly directions. NOGAPS and SAR based wind speeds compare well in most of the area.

The third Envisat ASAR wind map shown in Figure 52 is from 1 February 2009 with very strong winds from the east. In this wind map it is clear to see lee effects near coasts and islands. In the area with the strongest winds according to the SAR map, the NOGAPS model shows relatively weaker winds, otherwise the wind speeds agree well between NOGAPS and SAR.

7.2 Comparison to in situ data

The present work has included a study on how well NOGAPS wind directions compare with meteorological observations in the Baltic Sea.. The results are reported in detail in Hasager et al. (2011b). The key results are listed in Table 5. It is found that the wind direction from NOGAPS collocated with in situ wind directions compare well. Thus it is assumed that using NOGAPS wind directions a priori for SAR based wind retrieval is adequate. As found by Christiansen et al. (2006) SAR based winds are most accurately retrieved using in situ wind direction but this is generally not available. The study also compared SAR based wind speed to collocated in situ wind speed from the same offshore masts. These results are also listed in Table 5. The RMSE is 1.27 m s^{-1} which is better than the nominal accuracy of CMOD5 used in scatterometry wind retrieval. The bias is -0.25 m s^{-1} which means SAR winds are slightly negatively biased compared to the in situ winds.

Table 5: Comparison results of collocated NOGAPS wind direction to in situ observations of wind direction, and comparison results of collocated SAR wind speed to in situ observations of wind speed at 10 offshore meteorological masts in the Baltic Sea. N is number of samples, R^2 is correlation coefficient, SD standard deviation, RMS is root mean square error, and bias and slope are the results of the linear regression.

	Wind direction	Wind speed
N	927	875
R^2	0.950	0.783
SD	20.11°	1.88 m s^{-1}
RMS	6.29°	1.27 m s^{-1}
Bias	7.75°	-0.25 m s^{-1}
Slope	0.99	0.96

7.3 Wind resource mapping

Ocean wind resource mapping using SAR has been demonstrated in the North Sea (Christiansen et al., 2006; Hasager et al., 2004, 2006; Badger et al., 2010). The data set used for wind resource mapping in the South Baltic Sea consist of 1009 Envisat ASAR wind maps. Overview of the number of wind maps per year, per month, per season and time of day (day or night) is graphed in Figure 53. It is clear that most images are retrieved in years the years from 2007 to 2009, and that the images are fairly well spread between months and seasons, and that day and night acquisitions balance well. For seasons, the variation is from minimum 226 is summer to maximum 270 in winter. Figure 54 shows the number of images per month. The number varies around 25 since Risø DTU started near-real-time download from the ESA rolling archive in 2006 (Hasager et al., 2011a). Prior to this data were sent by DVD/ftp ad hoc.

Results from the SAR based study are shown in Figure 55. It is seen that the number of overlapping samples ranges from 400 to 600 in the study area that covers from 10° to 22° Eastern longitude and 54° to 59° Northern latitude. The Harlequin like pattern of the number of overlapping samples Figure 55 (top) is due to the orbital parameters of Envisat. Both ascending and descending scenes from morning and evening passes are combined, and this provides the pattern. Each swath is 400 km wide in the WSM. The domain is by far larger than the swath of the SAR. This means the resulting map is composed of different episodes of atmospheric conditions.

The map of mean wind speed in Figure 55 (middle) shows the offshore winds to range from 6 to 10 m s^{-1} in the study area. As expected the lowest winds found are close to

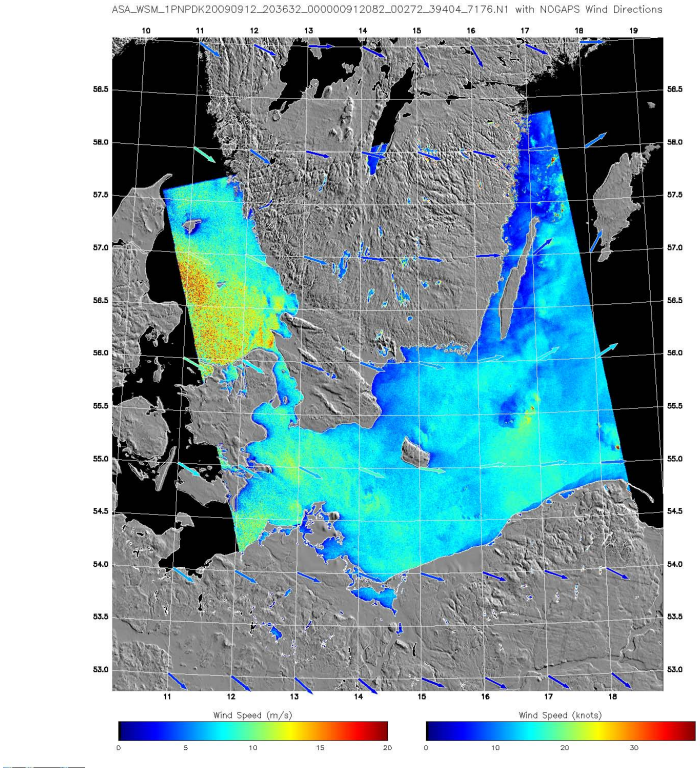

Figure 50: Envisat ASAR wind map from 12 September 2009 at 20:36 UTC in the Baltic Sea. The arrows are from the NOGAPS model.

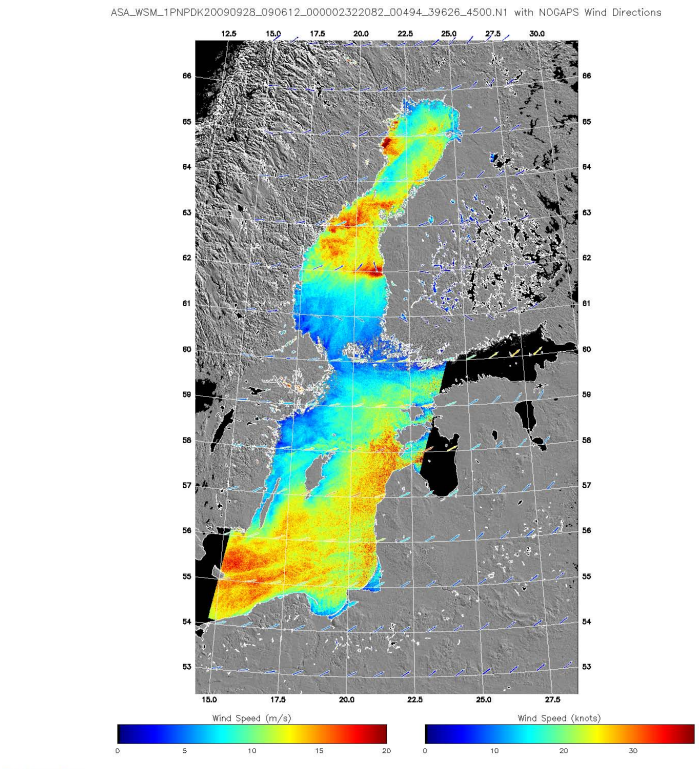

Figure 51: Envisat ASAR wind map from 28 September 2009 at 09:06 UTC in the Baltic Sea. The arrows are from the NOGAPS model.

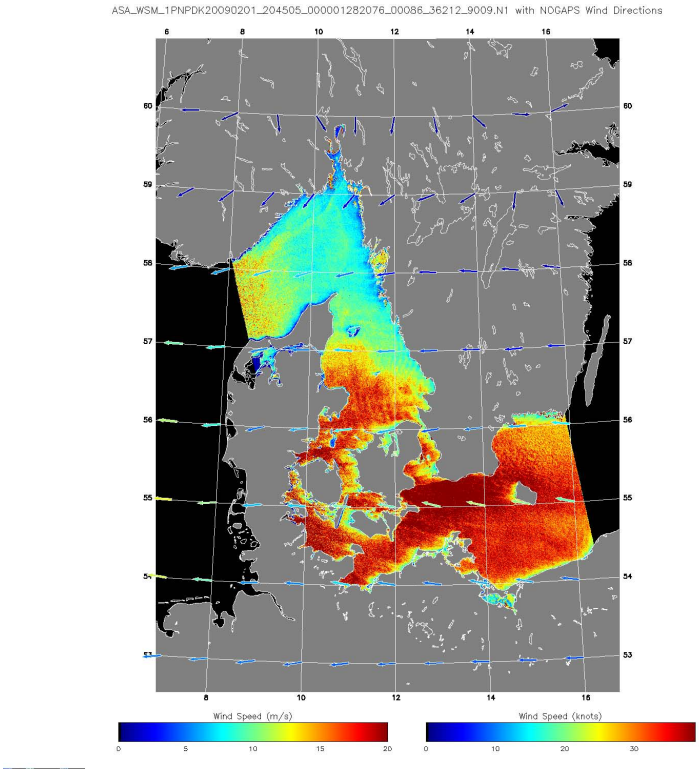

Figure 52: Envisat ASAR wind map from 1 February 2009 at 20:45 UTC in the Baltic Sea. The arrows are from the NOGAPS model.

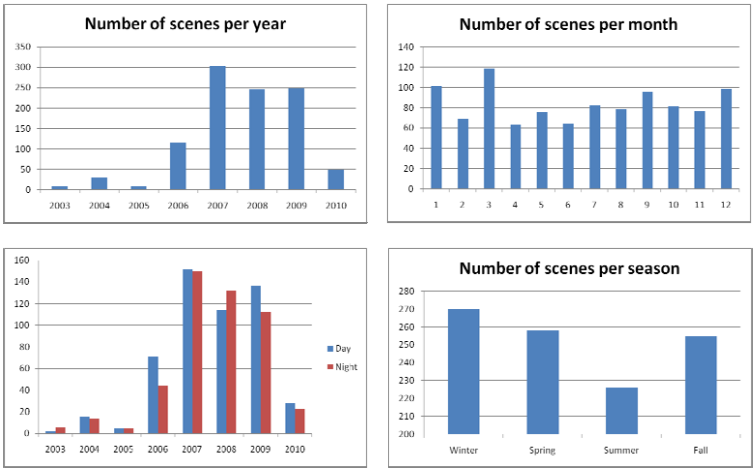

Figure 53: Histograms of the number of Envisat ASAR wind maps used in the analysis shown as function of year (top left), month (top right), day and night per year (bottom left) and per season (bottom right).

the coastline whereas the highest winds are in the central part of the South Baltic Sea.

The mean wind speed from 1960 to 1990 in Figure 55 (bottom), calculated by a working group within the World Meteorological Organization (WMO) is documented in WMO report 41. The WMO report is mainly based on ship, lighthouse and airport data from year 1960 to 1990 (Mietus, 1998). The WMO mean wind speed map is in knots whereas the SAR-based mean wind speed map is in ms-1. According to WMO map mean winds in most of the South Baltic Sea are above 14 knots ($\sim$7 m s^{-1}) but below 16 knots ($\sim$8 m s^{-1}). In the SAR-based map mean winds are between 8 and 9 m s^{-1}. Both maps show

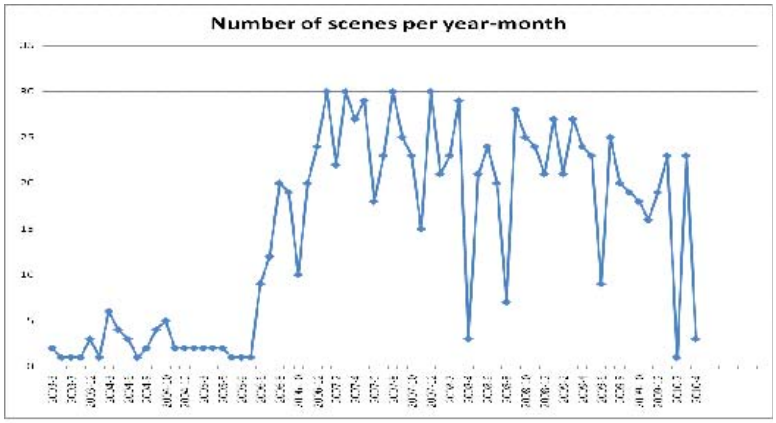

Figure 54: Time series of Risø DTU Envisat ASAR image acquisition per month over the South Baltic Sea.

higher winds in the Kattegat Strait, lower winds in the Great Belt, and maximum winds east of the island Bornholm. The near-coastal winds are mapped at around 6 m s^{-1} in both maps. It is striking that the maximum winds in the WMO map is 16 knots (∼8 m s^{-1}) in a small local area. In contrast, in the SAR-based mean wind speed map winds above 9 m s^{-1} found in a wide region central in the basin. The two methods of producing mean wind speed maps and also the time difference (1960 to 1990) vs. (2003 to 2010) are likely reasons for the discrepancies. The SAR maps is valid at 10 m. The WMO map is also near the surface.

In the SAR-based mean wind speed maps the following may be noticed: the data are at 1 km by 1 km resolution and no visual smoothing has been done for display. This means a slight 'salt and pepper' pattern appears. Also the orbital track is visible. This is caused by the different atmospheric conditions included across the domain.

Artifacts of retrieving ocean wind from radar are the following: hard targets such as ships, wind turbines, bridges, offshore platforms or tiny islands (that are not included in the basic land mask) will provide (much) higher radar backscatter within the grid cell and this will result in too 'high' wind speeds in the grid cell. This effect can be noticed at the Nysted 1 offshore wind farm (south of the island Lolland), along the Great Belt bridge between the islands Zealand and Funen, and along the Øresund bridge between Copenhagen and Malmö. South of the latter bridge the Lillgrund offshore wind farm is visible. Slightly more subtle but clear when noticed is the S-shape track of the large container ship route from the Baltic Sea through the Great Belt. Also the ferry link Rødby to Puttgarten is seen as short straight line.

Despite the above mentioned artifacts the Envisat ASAR wind map data set has been used for calculation of wind resource statistics: the Weibull scale (A) and shape (k) parameters and the wind energy density. The Weibull results are shown in Figure 56 and energy density in Figure 57. Weibull A ranges from 7 to 11 m s^{-1} with a smooth appearance. Weibull k ranges from 1.2 to 2.2 with a non-smooth appearance. The reason for the two results are that relatively few samples are needed in order to estimate Weibull A accurately while many more samples are need to estimate Weibull k. This means that due to the number of samples Weibull k is more uncertain (Barthelmie and Pryor, 2003; Pryor et al., 2004)

Figure 57 shows the energy density to range from 200 to 1200 W m^{-2}. In the analysis by Hasager et al. (2011b) the wind energy density and Weibull A and k were compared with data from one meteorological mast, the Fino2 mast, in the Baltic Sea. The comparison results were not as good as those found by Badger et al. (2010) in the North Sea using three masts and approximately the same number of Envisat ASAR wind maps all processed in the same way. In the North Sea study the mean wind speed and Weibull

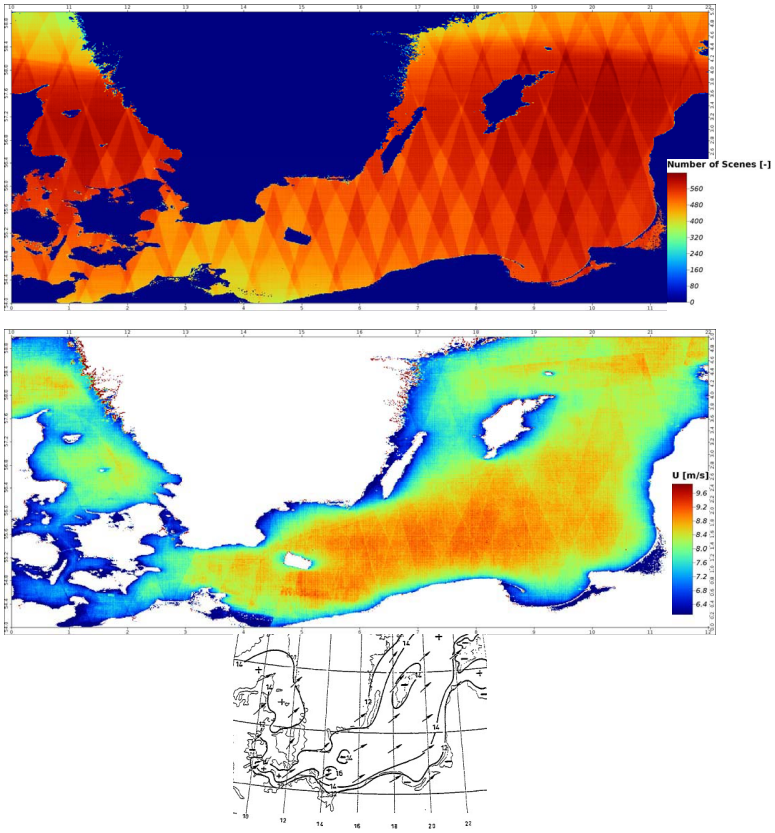

Figure 55: Envisat ASAR number of overlapping maps (top) and mean wind speed (middle) for the South Baltic Sea. The bottom figure shows mean wind speed in knots and directions from the period 1960 to 1990 (Mietus, 1998).

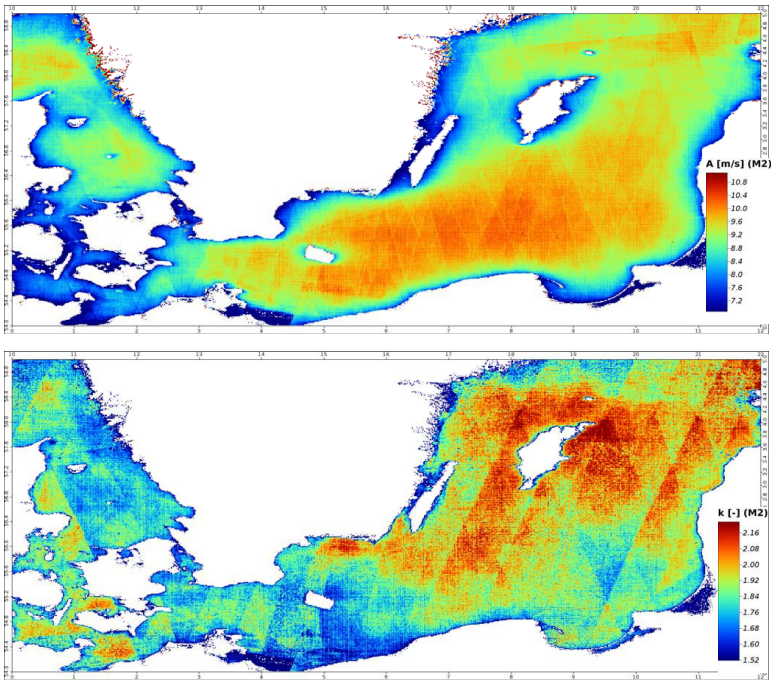

Figure 56: Envisat ASAR Weibull A (top) and Weibull k (bottom) the South Baltic Sea.

A were both estimated within $\sim 5\%$ and Weibull k and energy density within $\sim 7\%$. In the Baltic Sea comparison the results on mean wind speed and Weibull A were within the same range whereas Weibull k and energy density ranged from 16 to 29% depending on the chosen fitting function for the Weibull statistics. In the present report, the results are from the 2.order moments method.

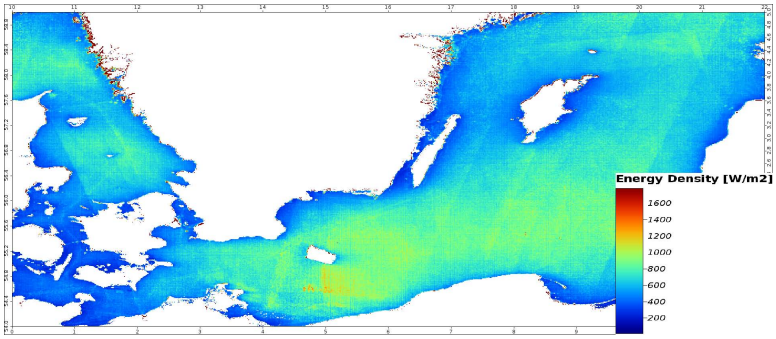

Figure 57: Envisat ASAR wind energy density in the South Baltic Sea.

Several wind farms are located in the South Baltic Sea and many more are in planning. The existing offshore wind farms and plans can be viewed at the website: http://www.4coffshore.com/windfarms/. In the study in Hasager et al. (2011b) the SAR-based results showed energy density to range between 300 to 800 W m^{-2}. It was in particular noticed that all existing wind farms are located less than 15 km offshore and the variability in energy density is very large, ranging from 300 to 700 W m^{-2} in this zone. Further offshore higher and more constant energy density was found.

7.4 Summary

SAR based wind resource estimation analyzing 1009 Envisat ASAR wind maps are presented. The results are valid at 10 m above sea level and therefore the results may be used to evaluate model results at the same level. Alternatively, the wind maps may give pre-feasibility information on the offshore wind resource. From the results it is clear that the near-coastal zone experience large wind gradients in the South Baltic Sea. The high spatial resolution of 1 km by 1 km of SAR ocean wind maps is an advantage. The limitation is the relatively few numbers of observations at two fixed times of the day. Thus additional work needs to be done to capture a likely 20-year wind resource at hub-height.

8 Wind atlas

8.1 Downscaling methodology

The WRF simulations use the dynamical downscaling technique developed by Hahmann et al. (2010), but using Newtonian relaxation towards the large scale analysis (also known as grid nudging or analysis nudging). Newtonian relaxation is accomplished by adding non-physical nudging terms to the WRF predictive equations (i.e. wind components, temperature, and specific humidity). These terms force the model solution at each grid point to the global analysis in proportion to the difference between the model solution and the global analysis. The result of this procedure is that the model solution is constrained by the large-scale analysis, but allowed to develop mesoscale circulations. Nudging terms are only applied above level 10 and thus do not interfere with the development of the boundary layer.

Maps of mean wind speed for the period 2007–2009 are presented in Figures 58, 59, and 60, for 80, 100, and 125 m AGL, respectively. Vertical interpolation between model levels has been used to compute wind speeds at these levels. Within the Baltic Sea, wind speeds are larger in the western part south of Sweden and in the area east and north of Bornholm.

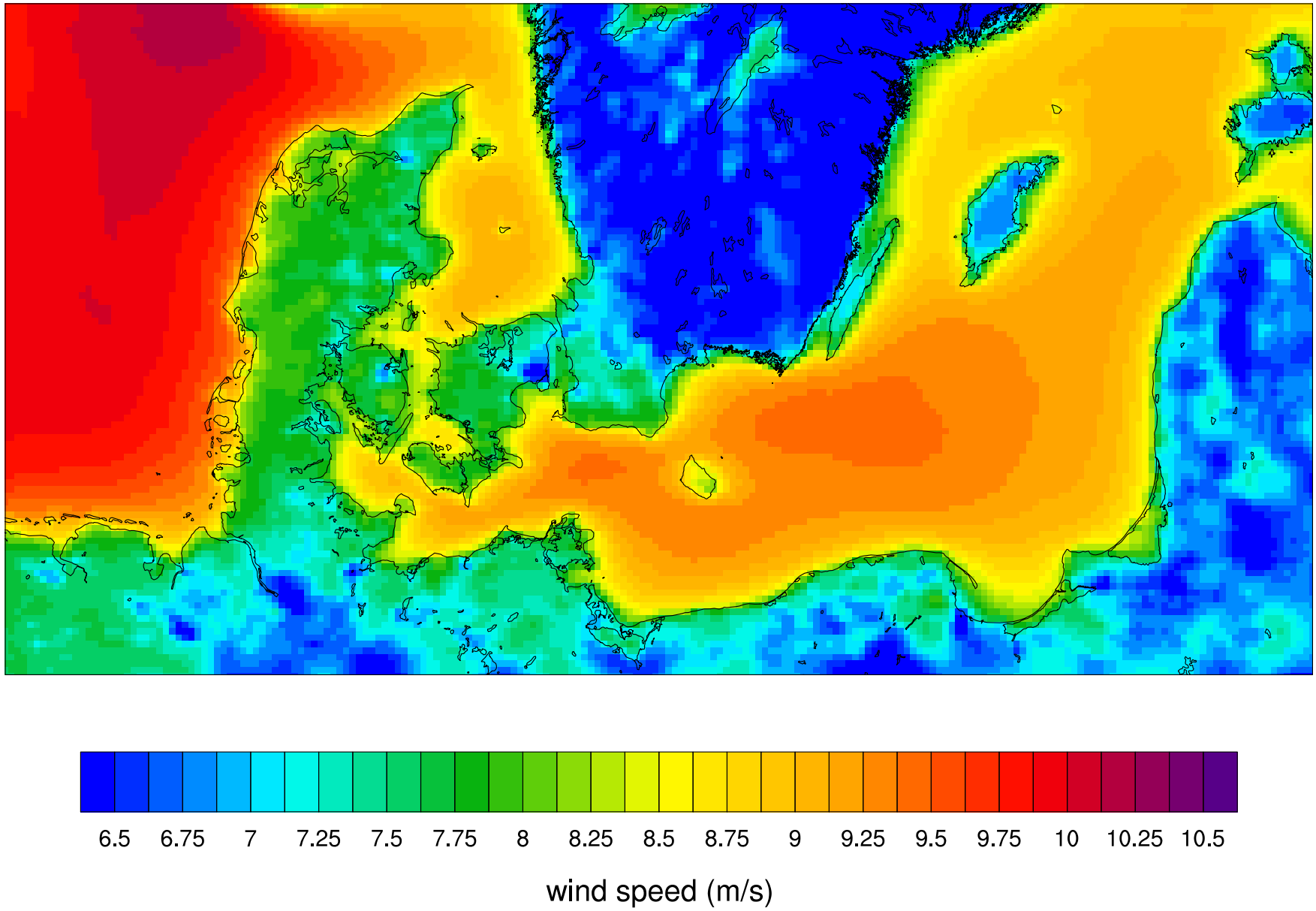

Figure 58: Averaged wind speed simulated by WRF for the period 2007–2009 and interpolated to the level of 80meters.

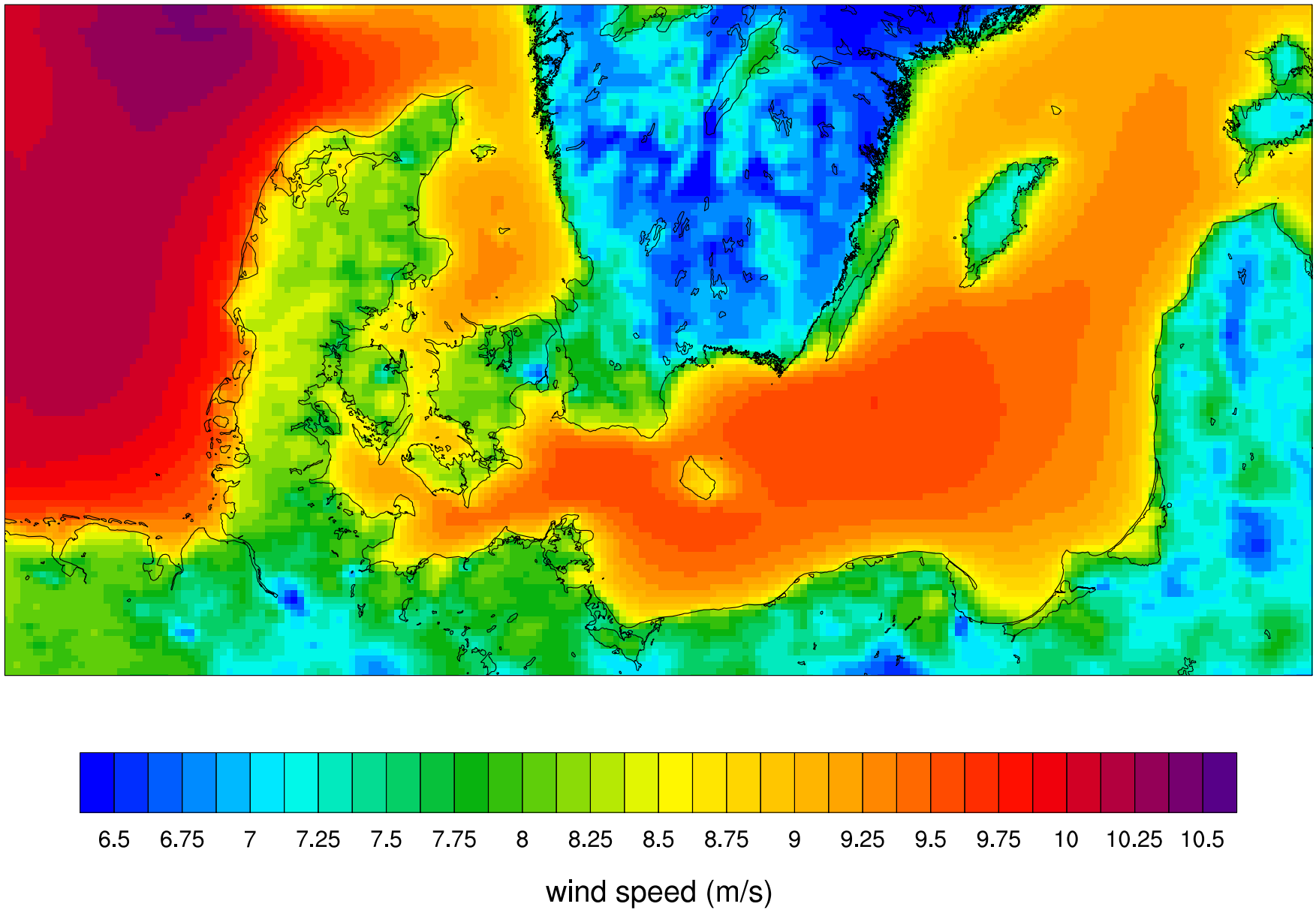

Figure 59: Averaged wind speed simulated by WRF for the period 2007–2009 and interpolated to the level of 100 m.

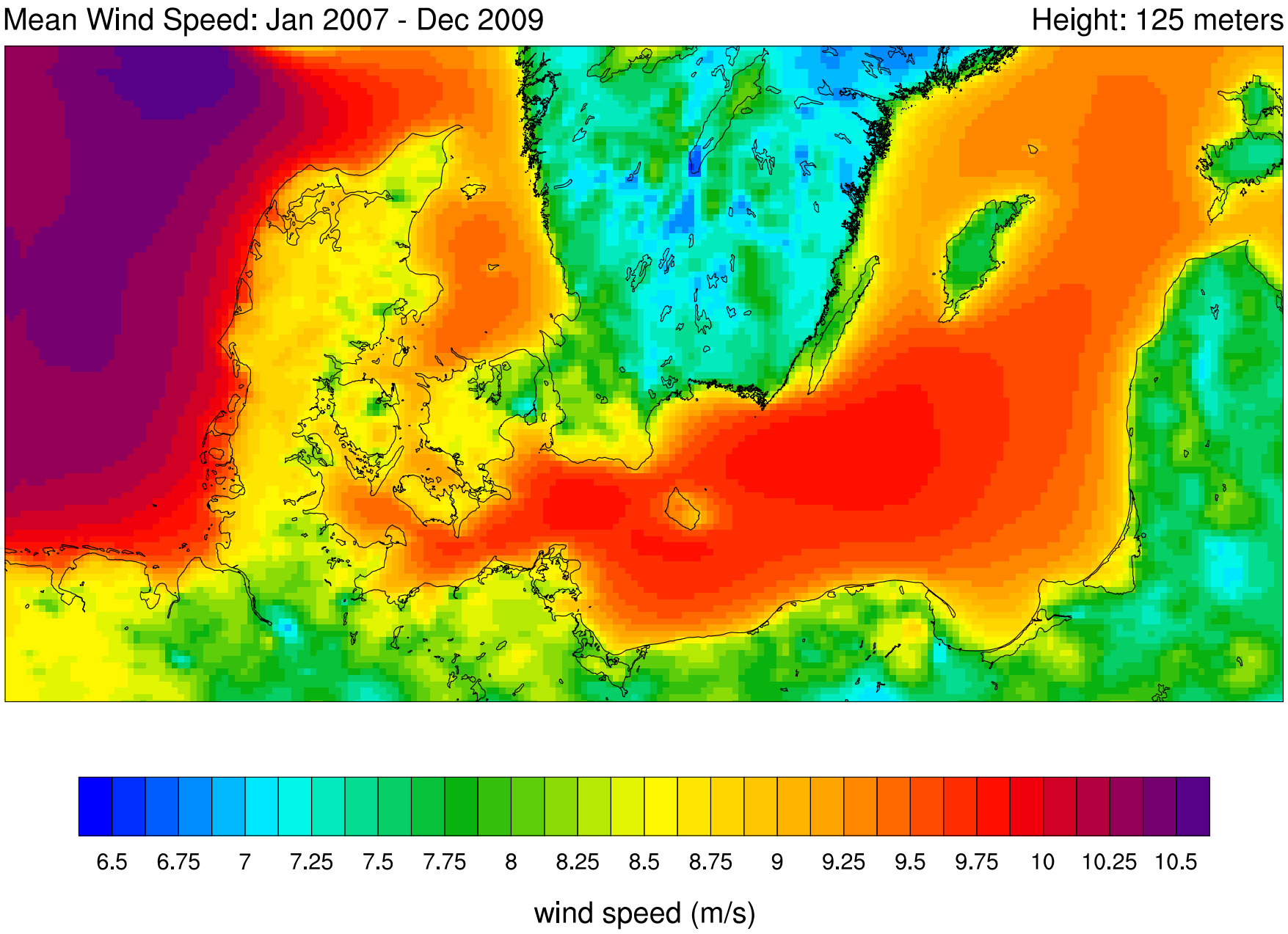

Figure 60: Averaged wind speed simulated by WRF for the period 2007–2009 and interpolated to the level of 125 m.

8.2 Wind Class Sampling

The WRF downscaling simulation covers a relatively short period (2007–2009). Therefore, to obtain a representative long-term annual-mean wind resource map, one needs to account for inter-annual changes in atmospheric flow conditions. In this project we attempt to use a new technique that combines the dynamical WRF downscaling with wind classes derived from NCEP/NCAR reanalysis data. A description of how the wind classes were obtained is presented in Section 4.

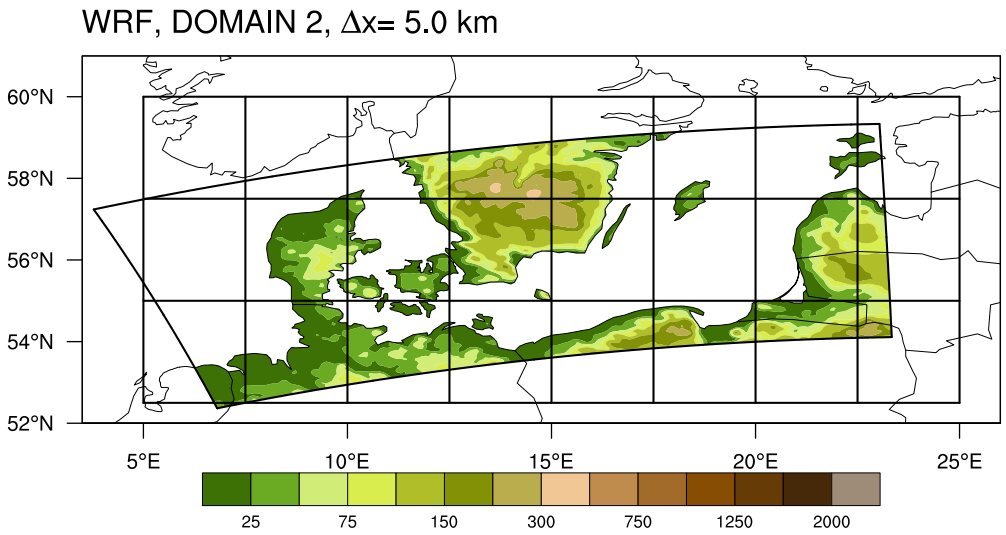

Figure 61: Location of NCEP/NCAR reanalysis boxes with relation to the WRF simulation domain.

We quickly outline the method used to weight the WRF data here. The region of interest (Figure 61) is covered by 21 NCEP/NCAR reanalysis grid squares ($K = 1 - 21$) $2.5° \times 2.5°$ in size from 7.5°–25° E and 52.5°–60° N. For this application wind classes are determined using time series (every 6 hours for the period 1980–2009) of the geostrophic wind and Froude number for all 21 NCEP/NCAR grid squares in order to represent all possible atmospheric states in the region of interest. The analysis results in $N = 137$ wind classes.

The averaged wind speed for wind class n at NCEP/NCAR reanalysis grid square K is computed from

$$V_{ij}^{K}(n) = \frac{1}{M(n)} \sum_{m=1}^{M(n)} V_{ij}(t_m),$$

where $M(n)$ is the total number of samples of wind class n in the simulation period (2007–2009), and (i, j) is a WRF grid point contained within the NCEP/NCAR reanalysis grid square K. Each value, $V_{ij}(t_m)$, represents a weighted mean of 7 hourly times centered (i.e. 3 hours before and 3 hours after) the valid time of the NCEP/NCAR reanalysis. From this value the long-term adjusted wind speed at NCEP/NCAR reanalysis grid square K can be computed from

$$\overline{V_{ij}^{K}} = \frac{\sum_{n=1}^{N} V_{ij}^{K} f^{K}(n)}{\sum_{n=1}^{N} f^{K}(n)},$$

where $f^{K}(n)$ is the frequency of occurrence of wind class n at NCEP/NCAR reanalysis grid point K. These weights are determined from the occurrence of the class within the full 30-year NCEP/NCAR reanalysis. Finally, all the V_{ij}^{K} are composited together to form a continuous map of the long-term average wind speed on the original WRF grid. At the

moment the weights are kept constant within each NCEP/NCAR reanalysis grid square. A consistent way of interpolating them is under development.

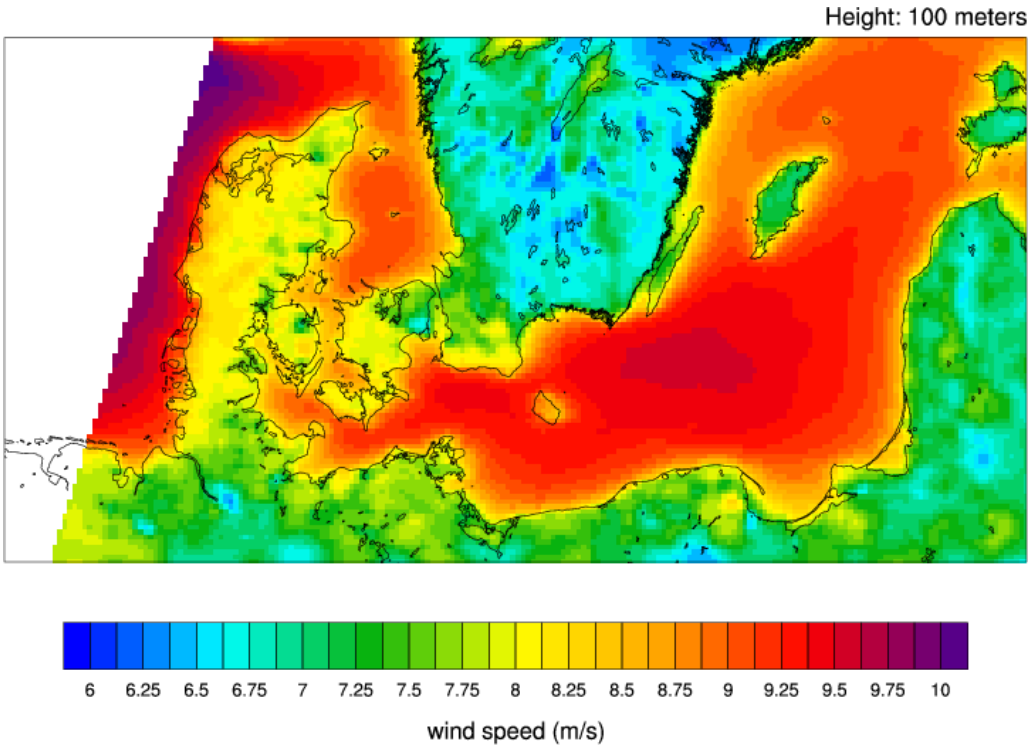

Figure 62: Long-term average wind speed at 100 m computed from the experimental wind class sampling method.

Figure 62 presents such a map for the 100-m long-term average wind speed. The difference between this long-term average wind speed and the simple average of the 2007–2009 wind speed (Figure 59) is presented in Figure 63. The figure shows mostly negative values, which implies that in this region the long-term mean wind speed is slightly lower (by 0–0.3 m s^{-1}) than that estimated from the 2007–2009 average. The boundaries of the NCEP/NCAR reanalysis grid squares are clearly visible in this figure, especially in the north-south direction. This is an artifact of the assumption of uniform representativeness of the wind classes on each NCEP/NCAR reanalysis grid square. A method for removing this problem is currently under development.

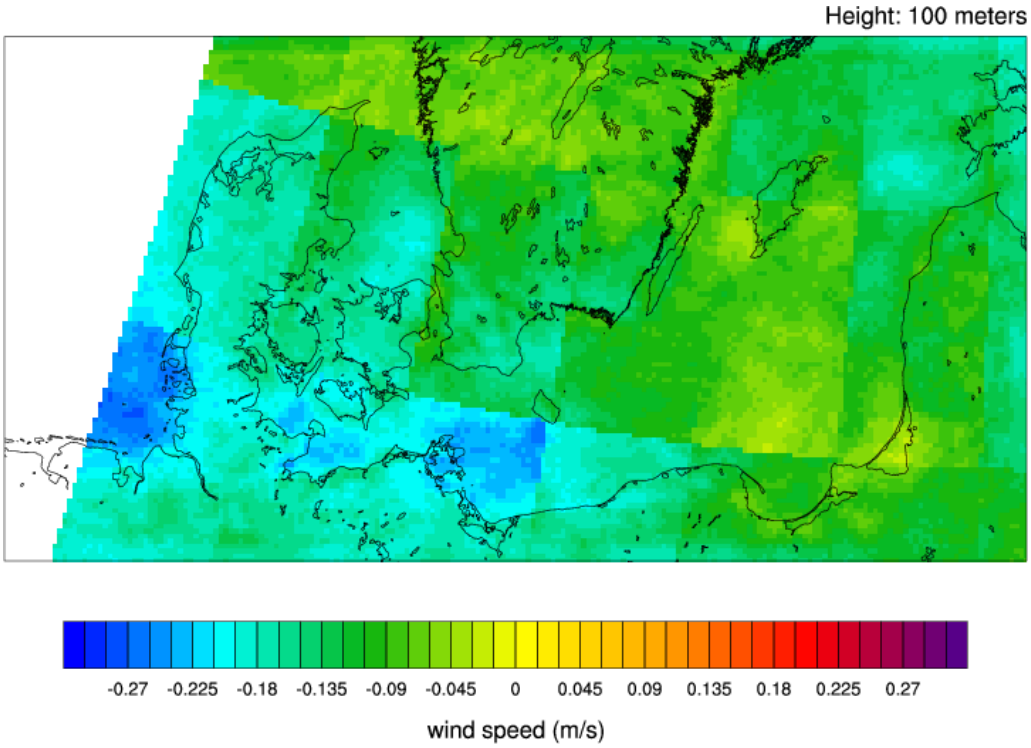

Figure 63: Difference between the long-term average wind speed at 100 me computed from the experimental wind class sampling method (Figure 62) and the simple 2007–2009 wind speed average.

9 Observed wind climate at Fino2

We supply here a so-called observed wind climate (OWC) based on the observations at Fino2 at the top cup anemometer as an example. The OWC can be directly used by the Wind Atlas Analysis and Application Program (WAsP) to perform wind energy analysis and resource assessment studies. In Tables 6–8 and Figure 64 are the main characteristics of the OWC file (also known as TAB files):

Table 6: All-sectors statistics of the OWC at Fino2 for the 102 m height

	Weibull-A [m s^{-1}]	Weibull-k ´	Mean wind speed [m s^{-1}]	Power density [W m^{-2}]
Source data(97484)	-	-	9.90	987
Fitted	11.3	2.47	10.04	988
Emergent	-	-	10.00	988
Combined	11.3	2.42	10.00	989

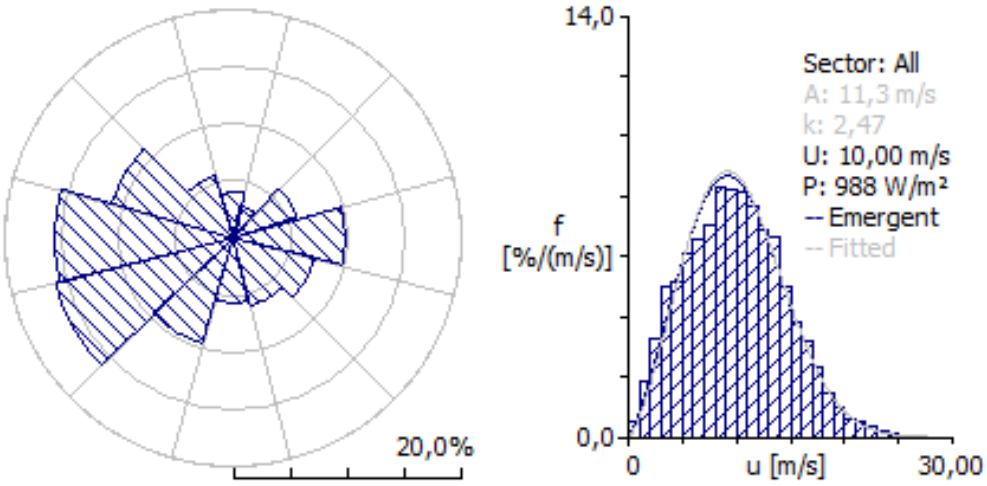

Figure 64: Wind rose and wind speed distribution of all sectors at Fino2 for the 102 m height.

Table 7: Per-sector statistics of the OWC at Fino2 for the 102 m height

	0	30	60	90	120	150	180	210	240	270	300	330
A	8,5	7,8	11,4	11,5	10,2	10,5	10,7	12,1	12,5	12,2	11,6	9,2
k	2,16	2,09	2,61	2,99	2,27	2,41	2,38	2,87	2,75	2,52	2,33	1,94
U	7,53	6,93	10,17	10,27	9,04	9,26	9,46	10,78	11,08	10,87	10,25	8,16
P	464	374	986	934	768	790	850	1106	1234	1235	1097	656
f	4,1	3,1	5,8	9,9	7,4	6	5,7	9,6	16,1	15,6	11	5,7

The 4 year WRF simulation runs can similarly be used in WAsP. The 4-year WRF long-term corrected time series of wind speed and direction can be inserted in WAsP as an OWC file (for one grid point at one height at the time) together with a digital map

Table 8: Per-sector and per wind speed bin statistics of the OWC at Fino2 for the 102 m height

U	0	30	60	90	120	150	180	210	240	270	300	330	All
1	7	10	5	3	5	9	12	5	3	3	3	7	5
2	37	44	20	14	19	22	31	17	13	13	14	26	19
3	56	91	40	28	45	34	42	31	21	20	24	42	33
4	100	133	63	30	56	75	55	44	32	31	47	72	50
5	92	95	53	39	56	65	61	44	34	32	61	84	51
6	106	84	56	46	74	64	65	51	45	52	70	92	61
7	85	87	62	55	80	75	68	60	47	55	75	106	66
8	101	67	60	63	82	70	71	73	60	63	75	101	71
9	107	95	78	97	112	89	90	64	75	73	73	98	83
10	82	83	61	110	82	92	60	60	85	94	69	86	82
11	56	66	82	95	86	82	51	71	95	99	68	62	81
12	48	57	99	87	81	56	69	62	91	92	73	45	77
13	35	33	88	81	51	66	71	83	73	76	66	45	69
14	30	25	83	79	43	64	75	95	74	64	68	39	67
15	27	15	47	51	25	38	71	76	66	45	52	29	50
16	10	5	25	47	22	28	51	57	46	43	41	16	38
17	7	5	15	40	30	27	23	39	41	40	37	15	32
18	7	4	12	21	25	20	17	25	32	32	29	12	24
19	6	0	10	9	13	15	6	14	22	22	19	6	15
20	2	0	9	4	8	7	3	14	19	15	9	5	10
21	0	0	8	1	4	2	5	8	10	11	6	3	6
22	0	0	11	0	1	1	1	3	7	10	7	2	5
23	0	0	8	0	0	0	1	2	5	7	6	2	3
24	0	0	4	0	0	0	0	1	2	4	3	2	2
25	0	0	0	0	0	0	0	0	0	2	3	2	1
26	0	0	0	0	0	0	0	0	0	1	2	2	0
27	0	0	0	0	0	0	0	0	0	0	1	1	0
28	0	0	0	0	0	0	0	0	0	0	0	0	0

containing the orography and roughness information of WRF around that grid point to produce a generalized/regional wind climate (RWC). The RWC, valid for a region of 5–20 km, can be used in WAsP to predict the wind resource by using a well-detailed digital map of the point of interest. This is the European Wind Atlas methodology (Troen and Petersen, 1989).

10 Conclusions

The aim is to provide a wind atlas for the South Baltic Sea. This has been performed using the WRF mesoscale model and the results are reported. This method was selected as meteorological observations are sparse.

Data from Danish and German masts were used for comparison to the WRF results and only data from tall masts were used as one of the key problems is to extrapolate from surface to hub-height of the foreseen offshore wind turbines. Six different boundary-layer parametrization schemes were evaluated for a one-month period comparing WRF results to observed wind profiles at the masts to select a suitable scheme.

Observations from Earth observing satellites were collected to provide means for spatial evaluation of the WRF model results near the surface. Around 7300 wind vector maps for a 10-year period from 1999 to 2009 from QuikSCAT scatterometer were retrieved and analyzed and 1000 Envisat ASAR wind maps from 2003 to 2011 were produced at Risø DTU and analyzed. The QuikSCAT and WRF results compared well whereas the Envisat ASAR mean wind map showed some variation to the others. The spatial resolutions are for SAR 1 km, WRF 5 km and QuikSCAT 25 km.

The WRF modeling was done in a nested domain of high spatial resolution for around 4 years. In addition the long-term wind statistics using the NCAR-NCEP reanalysis data were performed during 30 years to provide basis for a long-term adjustment of the results. The long-term analysis revealed that the South Baltic Sea has a spatially highly variable wind climate during the 30-years. The final WRF results include a weighting for the long-term trends variability in the South Baltic Sea. While the method used to derive the long-term average of wind speed appears to perform satisfactorily, there are no long-term observations in the area of the South Baltic to validate its accuracy. In addition, the extension of the use of the wind classes defined at a point to a large region requires further investigation.

It would be relevant to compare the results achieved with more observations to estimate the uncertainty.

11 Publication list

The following are a number of publications within the framework of the South Baltic project:

10. Hahmann, A. N. (2011) From trades to turbines – linking global, mesoscale, and local models, *EERA JP Wind: Wind Conditions Workshop*, Porto.

9. Karagali, I., Hasager, C. B., and Badger, M. (2011) Long-term wind characteristics in the North Sea and Baltic Sea from QuickSCAT gridded products, *Remote Sens. Environ.*, In review.

8. Hasager, C. B., Badger, M., Peña, A., Larsén, X. G., and Bingöl, F. (2011) SAR-based wind resource statistics in the Baltic Sea, *Remote Sens.*, **3**, 117–144.

7. Hahmann, A. N. (2011) Mesoscale models in wind energy: A quick guide *Conference of the European Wind Energy Association (EWEA)*, Brussels (Invited presentation)

6. Hasager, C. B., Badger, M., Badger, J., Bingöl, F., Clausen, N.-E., Hahmann, A., Karagali, I., and Peña, A. (2011) Combining satellite wind maps and mesoscale modelling for a wind atlas of the South Baltic Sea. *Conference of the European Wind Energy Association (EWEA)*, Brussels (abstract and poster)

5. Hasager, C. B., Badger, M, Badger, J., Nielsen, M. Bingöl, F., Hahmann, A. Karagali, I., and Peña, A. (2011) ASAR for offshore wind energy. *European Space Agency (ESA) Sentinel Potential Science Products for Cryosphere, Ocean, Land and Solid Earth Research Assessment and Consolidation Workshop*, Frascati(abstract and poster).

4. Hasager, C. B., Hahmann, A., Badger, J., Bingöl, F., Karagali, I., Peña, A., and Clausen, N.-E. (2011) Wind atlas mapping in the South Baltic Sea: methods and results. *European Geosciences Union (EGU) General Assembly*, Vienna, Geophysical Research Abstracts (ISSN: 1607-7962), vol: 13, pages: EGU2011-1339 (abstract and poster)

3. Hasager, C.B., Badger, J., Bingöl, F., Clausen, N.-E., Hahmann, A., Peña, A., and Badger, M. (2011) Wind energy resources of the South Baltic Sea. *Proceedings of the World Renewable Energy Conference (WREC)*, Linköbing (proceedings paper and oral presentation).

2. Hasager, C.B., Badger, M., Badger, J., Bingöl, F., Nielsen, M., Karagali, I., and Hahmann, A. (2011) Offshore wind resource mapping combining satellite winds and mesoscale modeling. *European Energy Research Alliance (EERA) Workshop on Wind Conditions,* Porto (poster)

1. Hasager, C., Hahmann, A., Badger, J., Bingöl, F., Peña, A., Karagali, I., Clausen, N.-E., and, Badger, M. (2011) Winds in the South Baltic Sea - working towards a wind atlas. *European Wind Energy Association (EWEA) Offshore*, Amsterdam (abstract submitted)

References

A.B. Kara, P. M., A.J. Wallcraft and R. Pauley, 2009: Optimizing surface winds using quikscat measurements in the mediterranean sea during 2000-2006. *Journal of Marine Systems*, **78**, 119–131.

Badger, M., J. Badger, M. Nielsen, C. B. Hasager, and A. Peña, 2010: Wind class sampling of satellite SAR imagery for offshore wind resource mapping. *J. Applied Meteorol. Climatol.*, **49**, 2474–2491.

Barthelmie, R. J. and S. C. Pryor, 2003: Can satellite sampling of offshore wind speeds realistically represent wind speed distributions. *J. Appl. Meteorol.*, **42**, 83–94.

Bougeault, P. and P. Lacarrère, 1989: Parameterization of orography-induced turbulence in a mesobeta-scale model. *Mon. Wea. Rev.*, **117**, 1872–1890.

B.R. Furevik, L. C. J.-M. L. C. T., A.M. Sempreviva, 2010: Eight years of wind measurements from scatterometer for wind resource mapping in the mediterranean sea. *Wind Energy*.

C. Accadia, A. L., S. Zecchetto and A. Speranza, 2007: Comparison of 10-m wind forecasts from a regional area model and quikscat scatterometer wind observations over the mediterranean sea. *Monthly Weather Review*, **135**, 1945–1960.

Chelton, D. B. and M. Freilich, 2005: Scatterometer-based assessment of 10-m wind analyses from the operational ecmwf and ncep numerical weather prediction models. *Mon. Wea. Rev.*, **133**, 409–429.

Christiansen, M. B., C. B. Hasager, D. R. Thompson, and F. Monaldo, 2008: Ocean winds from synthetic aperture radar. in *Ocean Remote Sensing Techniques and Applications*, niclos r., caselles v. eds. Tech. rep., Research Singpost Editorial.

Christiansen, M. B., W. Koch, J. Hortsmann, and C. B. Hasager, 2006: Wind resource assessment from C-band SAR. *Remote Sensing of Environm.*, **105**, 68–81.

D.B. Chelton, J. S., M.H. Freilich and J. V. Ahn, 2006: On the use of quikscat scatterometer measurements of surface winds for marine weather prediction. *Mon. Wea. Rev.*, **134**, 2055–2071.

Draxl, C., A. N. Hahmann, A. Peña, and G. Giebel, 2011: Comparison of wrf boundary-layer parameterizations for wind energy forecasting. *Wind Energ.*, in review.

Frank, H. P., O. Rathmann, N. G. Mortensen, and L. Landberg, 2001: The numerical wind atlas – the KAMM/WAsP method. Tech. Rep. Risoe-R-1252(EN), Risø National Laboratory, Roskilde.

Hahmann, A. N., D. Rostkier-Edelstein, T. T. Warner, F. Vandenberghe, Y. Liu, R. Babarsky, and S. P. Swerdlin, 2010: A reanalysis system for the generation of mesoscale climatographies. *J. Applied Meteorol. Climatol.*, **49**, 954–972.

Hasager, C. B., J. Badger, F. Bingöl, N. E. Clausen, A. Hahmann, I. Karagali, M. Badger, and A. Peña, 2011a: Wind energy resources of the Sout Baltic Sea. *Proc. of World Renewable Energy Conference (WREC)*, Linköbing.

Hasager, C. B., M. Badger, A. Peña, X. G. Larsén, and F. Bingöl, 2011b: Sar-based wind resource statistics in the Baltic Sea. *Rem. Sens.*, **3**, 117–144.

Hasager, C. B., R. J. Barthelmie, M. B. Christiansen, M. Nielsen, and S. C. Pryor, 2006: Quantifying offshore wind resources from satellite wind maps: study area the North Sea. *Wind Energy*, **9**, 63–74.

Hasager, C. B., E. Dellwik, M. Nielsen, and B. Furevik, 2004: Validation of ERS-2 SAR offshore wind-speed maps in the North Sea. *Int. J. Rem. Sens.*, **25**, 3817–3841.

Hersbach, H., A. Stoffelen, and S. de Haan, 2007: An improved C-band scatterometer ocean geophysical model function:CMOD5. *Journal of Geophysical Research*, **112(C03006)**.

Hoffman, R. and S. Leidner, 2005: An introduction to the near-real-time quikscat data. *Weather and Forecasting*, **20**, 476–493.

Hong, S.-Y., Y. Noh, and J. Dudhia, 2006: A new vertical diffusion package with an explicit treatment of entrainment processes. *Mon. Wea. Rev.*, **134**, 2318–2341.

J. Boutin, L. M., Y. Quilfen and J. Piolle, 2009: Global average of air-sea co2 transfer velocity from quikscat scatterometer wind speeds. *J. Geophys. Res.-Oceans*, **114**.

J. Winterfeldt, C. K. S. B., A. Andersson and R. Weisse, 2010: Comparison of hoaps, quikscat and buoy wind speed in the eastern north atlantic and the north sea. *IEEE Transactions on Geoscience and Remote Sensing*, **48(1)**, 338–347.

Janjic, Z. I., 2001: Nonsingular implementation of the Mellor-Yamada level 2.5 scheme in the NCEP Meso model. Tech. rep., National Centers for Environmental Prediction: Camp Springs, MD, USA.

K. Satheesan, A. P. M. R. K., A. Sarkar and Y. Kuroda, 2007: Comparison of wind data from quikscat and buoys in the indian ocean. *Int. J. of Remote Sensing*, **28(10)**, 2375–2382.

Kanamitsu, M., W. Ebisuzaki, J. Woollen, S. K. Yang, J. J. Hnilo, and M. Fiorino, 2002: Ncep-doe amip-ii reanalysis (r-2). *Bull. Am. Meteorol. Soc.*, **83**, 1631–1643.

Kolstad, E., 2008: A quikscat climatology of ocean surface winds in the nordic seas: Identification of features and comparison with the ncep/ncar reanalysis. *Journal of Geophysical Research*, **113**.

Liu, W. T., 2002: Progress in scatterometer application. *Journal of Oceanography*, **58**, 121–136.

Liu, W. T. and W. Tang, 1996: Equivalent neutral wind. *National Aeronautics and Space Administration, Jet Propulsion Laboratory, California Institute of Technology, National Technical Information Service, distributor.*

M. A. Bourassa, J. J. O., D. M. Legler and S. R. Smith, 2003: Seawinds validation with research vessels. *J. Geophys. Res.*, **108(C2)**, 3019.

Mellor, G. L. and T. Yamada, 1982: Development of a turbulence closure model for geophysical fluid problems. *Rev. Geophys. Space Phys.*, **20**, 851–875.

M.H. Pickett, L. R., W. Tang and C. Wash, 2003: Quikscat satellite comparisons with nearshore buoy wind data off the u.s. west coast. *Journal of Atmospheric and Oceanic Technology*, **20**, 1869–1879.

Mietus, M., 1998: *The climate of the Baltic Sea Basin.* World Meteorological Organization.

Monaldo, F., 2000: The alaska sar demonstyration and near-real-time synthetic aperture radar winds. *John Hopkins APL Technical Digest*, **21**, 75–79.

Monaldo, F., et al., 2003: The sar measurement of ocean surface winds:an overview. *Proc. of the Second Workshop Coastal and Marine Applications of SAR*, Svalbard.

N. Ebuchi, H. G. and M. Caruso, 2002: Evaluation of wind vectors observed by quikscat \seawinds using ocean buoy data. *Journal of Atmospheric and Oceanic Technology*, **19**, 2049–2062.

Nakanishi, M. and H. Niino, 2006: An improved mellor-yamada level-3 model: Its numerical stability and application to a regional prediction of advection fog. *Bound.-Layer Meteor.*, **119**, 397–407.

Niros, A., T. Vihma, and J. Launiainen, 2002: Marine meteorological conditions and air-sea exchange processes over Northern Baltic Sea in 1990s. *Geophysica*, **38**, 59–88.

Nygaard, I., et al., 2010: Using modeling, satellite images and existing global datasets for rapid preliminary assessments of renewable energy resources: the case of Mali. *Renewable & Sustainable Energy Reviews*, **14**, 2359–2371.

Pryor, S. C., M. Nielsen, R. J. Barthelmie, and J. Mann, 2004: Can satellite sampling of offshore wind speeds realistically represent wind speed distributions? part ii quantifying uncertainties associated with sampling strategy and distribution fitting methods. *J. Appl. Meteorol.*, **43**, 739–750.

Reynolds, R. W., N. A. Rayner, T. M. Smith, D. C. Stokes, and W. Q. Wang, 2002: An improved in situ and satellite sst analysis for climate. *J. Climate*, **15**, 1609–1625.

Risien, C. and D. Chelton, 2006: A satellite-derived climatology of global ocean winds. *Remote Sensing of Environment*, **105(3)**, 221–236.

S. Pensieri, R. B. and M. Schiano, 2010: Comparison between quikscat and buoy wind data in the ligurian sea. *Journal of Marine Systems*, **81**, 286–296.

Saha, S., et al., 2010: The NCEP climate forecast system reanalysis. *Bull. Amer. Meteor. Soc.*, **91**, 1015–1057.

Skamarock, W. C., et al., 2008: A description of the advanced research wrf version 3. Tech. Rep. NCAR/TN-475+STR, Mesoscale and Microscale Meteorology Division, National Center for Atmospheric Research, Boulder, Colorado, USA, 113 pp.

Sukoriansky, S., B. Galperin, and V. Perov, 2006: A quasi-normal scale elimination model of turbulence and its application to stably stratified flows. *Nonlinear Process. Geophys.*, **13**, 9–22.

Troen, I. and E. L. Petersen, 1989: European wind atlas. Tech. rep., Risø National Laboratory.

W. Tang, W. L. and B. Stiles, 2004: Evaluation of high-resolution ocean surface vector winds measured by quikscat scatterometer in coastal regions. *IEEE Transactions on Geoscience and Remote Sensing*, **42**, 1762–1769.

Zecchetto, S. and F. D. Biasio, 2007: Sea surface winds over the mediterranean basin from satellite data (2000-04): Meso- and local-scale features on annual and seasonal time scales. *J. Appl. Meteor. Climatol.*, **46**, 814–827.

Risø DTU is the National Laboratory for Sustainable Energy. Our research focuses on development of energy technologies and systems with minimal effect on climate, and contributes to innovation, education and policy. Risø has large experimental facilities and interdisciplinary research environments, and includes the national centre for nuclear technologies.

Risø DTU
National Laboratory for Sustainable Energy
Technical University of Denmark

Frederiksborgvej 399
PO Box 49
DK-4000 Roskilde
Denmark
Phone +45 4677 4677
Fax +45 4677 5688

www.risoe.dtu.dk